



# Characteristics and Precursor of Static and Dynamic Triggered Rockburst: Insight from Multifractal

Fuqiang Ren<sup>1,2</sup> · Chun Zhu<sup>2,3,5</sup> · Manchao He<sup>2,3</sup> · Junlong Shang<sup>4</sup> · Guangliang Feng<sup>5</sup> · Jinwen Bai<sup>6</sup>

Received: 9 March 2022 / Accepted: 20 November 2022 / Published online: 7 December 2022  
© The Author(s), under exclusive licence to Springer-Verlag GmbH Austria, part of Springer Nature 2022

## Abstract

To probe the difference between static-driven and dynamically triggered rockbursts, three types (static-driven rockburst, SDR; pulse-disturbance rockburst, PUDR; period-disturbance rockburst, PEDR) of true triaxial unloading rockburst tests were carried out on marble. The rockburst characteristics were compared and analyzed through five distinct aspects (stress–strain curve, energy consumption, failure mode, ejection features and acoustic emission (AE) multifractal characteristics). The results indicate that the rockburst stress values of the PUDR, the SDR and the PEDR decrease successively, which indicates that the PEDR and the PUDR are the most prone and the most difficult to occur, respectively. Additionally, the stress–strain curve (after yielding) data indicates that the PUDR, the SDR and the PEDR are characterized by a yield platform, strain hardening and strain softening, respectively. Moreover, the rockburst intensities of the PUDR, the SDR and the PEDR also decrease successively. Furthermore, the initial increase and the subsequent decrease of the AE multifractal parameter ( $\Delta f$  ( $\alpha$ )) can be used as the precursor for the different types of rockbursts. However, the early warning time is related to the intensity of the rockburst, which implies that greater intensity values lead to a shorter early warning time. In general, the  $\Delta f$  ( $\alpha$ ) parameter and the stress drop can be used for long-term monitoring and short-impending prediction of rockburst, respectively.

**Keywords** Rockburst · Static-driven · Dynamic trigger · Multifractal · Stress drop

## Abbreviations

SDR	Static-driven rockburst	AF	Average frequency
PUDR	Pulse-disturbance rockburst	RA	Rise time divide by amplitude
PEDR	Period-disturbance rockburst	$\sigma_{10}, \sigma_{20}, \sigma_{30}$	Initial maximum, intermediate, minimal principal stress, respectively
AE	Acoustic emission	$\sigma_1, \sigma_2, \sigma_3$	Maximum, intermediate, minimal principal stress, respectively
MS	Microseismic	$U, U_e, U_r$	Total, elastic and residual strain energy, respectively
PIV	Particle image velocimetry	$U_{d1}, U_{d2}$	Dissipation energy before and during rockburst
		$\{T_i\}$	AE time series
		$\{P_i(n)\}$	Subset of AE time series with length $n$
		$x_q(n)$	Probability distribution of each subset
		$\tau(q)$	Quality index
		$q$	Weight factor
		$f(\alpha)$	Fractal dimension of the subset
		$\alpha$	Singularity index
		$\Delta T_1, \Delta T_2$	Early warning time of $\Delta f(\alpha)$ and stress drop

✉ Chun Zhu  
zhu.chun@hhu.edu.cn

<sup>1</sup> School of Civil Engineering, University of Science and Technology Liaoning, Anshan 114051, China

<sup>2</sup> State Key Laboratory for Geomechanics and Deep Underground Engineering, Beijing 100083, China

<sup>3</sup> School of Earth Sciences and Engineering, Hohai University, Nanjing 210098, China

<sup>4</sup> James Watt School of Engineering, University of Glasgow, Glasgow G12 8QQ, UK

<sup>5</sup> State Key Laboratory of Geomechanics and Geotechnical Engineering, Institute of Rock and Soil Mechanics, Chinese Academy of Sciences, Wuhan 430071, China

<sup>6</sup> College of Mining Engineering, Taiyuan University of Technology, Taiyuan 030024, China

## 1 Introduction

Rockburst hazards of underground tunnels surrounded by rocks in high stress areas are one of the most important phenomena that hinders the efficient development and utilization of underground mines and deep tunnels (Cai and Kaiser 2018; Amoussou et al. 2013). For example, the diversion tunnel of the Jinping II Hydropower Station has encountered multiple rockburst disasters during the construction process (Gong et al. 2012; Wang et al. 2012; Li et al. 2012). The Bayu tunnel in the Lalin section of the Sichuan-Tibet railway is considered one of the world's most severe rockburst tunnels (Yan et al. 2019), and the rockburst section accounts for 94% of the total length of the tunnel. Additionally, during the actual construction process, the rock mass surrounding the tunnel was continuously disturbed by excavation, mechanical, blasting vibration, fault dislocation and earthquake operations (Luo et al. 2021), which led to the generation of different types of rockbursts. Therefore, the study of static-driven (mainly affected by excavation) and dynamically triggered (the combined action of excavation and dynamic disturbance) rockbursts is of great importance for improving disaster prevention and control methods.

In recent years, several methods have been applied to study static-driven rockburst caused by the concentration of tangential stress after tunnel excavation operations. Among these, the true triaxial unloading rockburst experiment represents an important method that can help better understand the rockburst mechanism (He et al. 2010). The evolution process of rockburst (splitting into plates, shearing into blocks and block ejection) has been confirmed by rockburst experiments (Ren et al. 2020). The unique features of rockburst differentiated by the conventional compression failure technique were derived from the analysis of the ejection failure process, the failure mode, and the fragments' characteristics. Factors that influence rockbursts such as bedding orientation (He et al. 2012), size effect (Zhao and Cai 2014), unloading rate (Li et al. 2014), moisture content (Sun et al. 2016), temperature (Su et al. 2017a, b, c), stiffness effect (Cheng 2011), intermediate principal stress (Su et al. 2017a) and stress gradient (Huo et al. 2020; Hu et al. 2021) were studied by using the true triaxial rockburst technique. Additionally, the reduced-scale deep surrounding rock mass with holes (Luo et al. 2019; Gong et al. 2019, 2022) was selected as the reference object for carrying out physical simulation analyses of the true triaxial unloading rockburst for the representative elements of the rock mass, while the unloading state of the surrounding rock mass was simulated by drilling holes with different shapes in the cubic rock blocks to analyze the rockburst mechanism under true triaxial stress condition.

It is known that the magnitude of the strain rate has a significant impact on the rock failure mechanism (Dai et al. 2010), while the dynamically triggered rockburst is typically caused by the coupling effect of the static and dynamic loads. However, it is difficult to simulate the real stress conversion process of the rock mass surrounding the tunnel by the commonly used Splitting Hopkinson Pressure Bar experimental technique (uniaxial, triaxial and true triaxial tests) (Zhou et al. 2020; You et al. 2021). Therefore, it is more practical to simulate the dynamically triggered rockburst by the true triaxial unloading rockburst experimental test combined with the dynamic disturbance of the hydraulic loading mode. He et al. (2018) developed a deep rock nonlinear mechanics experimental system to simulate the rockburst of the rock mass surrounding the tunnel and analyzed the influence of different displacement disturbance amplitudes (0.1–0.5 mm), frequencies (0.05–1 Hz) and disturbance directions on the rockburst. Du et al. (2016) studied the influence of the lithology and the disturbance amplitude on the rock failure modes by using the static-dynamic combined loading test under true triaxial unloading conditions. In their test, the maximum disturbance frequency reached 70 Hz. Hu et al. (2018) also performed rockburst experiments characterized by weak disturbance attributes (far field disturbance, 2–50 Hz) under true triaxial conditions, and discussed the influence of disturbance amplitude, frequency, and disturbance mode on the rockburst.

The final goal of understanding the rockburst mechanism is to accurately predict rockburst disasters. Thus, the extraction and recognition of the rockburst precursor are crucial for the early detection of rockbursts (Ma et al. 2020). From an experimental point of view, the precursor of rockburst is primarily studied by applying AE, infrared and acoustic signals (Liu et al. 2018a, b). Usually, there are typical AE signals (high energy and small quantity) with an abnormal evolution, and the density of AE characteristic signals can be used as an early warning indicator (Liu et al. 2018a, b; Li et al. 2018a, b). The typical rockburst failure processes include particle ejection, block splitting and burst. Therefore, the infrared temperature field corresponding to different failure phenomena is different, which experiences initial differentiation, rapid rise of the differentiation degree, and then a brief decline and sudden decline of the differentiation degree (Lin et al. 2022). Additionally, the sound signals of the rockburst were first used to evaluate the intensity of the rockburst, specifically, the size and type of the generated sound were used to qualitatively describe rockbursts with different intensities (Chen et al. 2015). The research results of Su et al. (2017b) suggest that sparse to dense acoustic waves, high to low main frequencies, low to high energies recorded during the process of rockburst can be used as rockburst early warning indicators. In addition to the single

precursor characteristic, there are also multi-physical fields and multi-parameter rockburst precursors.

For field purposes, the microseismic (MS) technology is the most widely used method for rockburst monitoring and early warning, and is applied in hydraulic tunnels, railway tunnels, metal mines, coal mines and other similar projects (Lu et al. 2018; Tang et al. 2021; Wang et al. 2021a, b). In this case, the commonly used rockburst precursors are: the cumulative MS events and the cumulative MS energy release reach the corresponding thresholds (Li et al. 2019); concentration of a large number of MS events (Liu et al. 2018a, b); the sudden drop of the energy index and the sharp increase of the apparent volume or the seismic moment (Ma et al. 2020); the b-value of MS events initially increases and then decreases (Dai et al. 2017); the decline in the MS energy index, Schmitt number and the increase of the cumulative apparent volume (Zhang et al. 2016). However, the overall early warning success rate of various precursory indicators is low, and the reason is that the selected precursors are necessary rather than sufficient conditions for rockburst.

In summary, there are few reports that analyze the rockburst characteristics differences between static-driven rockburst (SDR) and dynamically triggered rockburst. Additionally, greater attention has been given to the long-term monitoring and early detection of rockburst, and less regarding the short-term and imminent prediction of rockburst. In this study, the SDR, pulse-disturbance rockburst (PUDR) and period-disturbance rockburst (PEDR) tests were carried out on marble samples by applying the true triaxial rockburst experimental system. Additionally, high-speed photography and AE monitoring systems were used to record

the ejection failure process and the micro-cracks evolution of the rockburst, respectively. The differences between the three types of rockburst characteristics were evaluated by comparing several aspects, such as the stress–strain curve, the energy dissipation, the failure mode, the ejection velocity field, and the AE multifractal characteristics. Consequently, the multifractal precursors of the three types of rockbursts were obtained. Finally, the mechanisms responsible for the different characteristics of the three types of rockbursts are examined, and the early warning concept of combining long-term monitoring with short-term and imminent prediction of rockburst is preliminarily reviewed. The main purpose of these analyses is to provide guidance for the prevention and control of rockburst disasters.

## 2 Material and Methods

### 2.1 Marble Samples

The marble samples used in this study were collected from the Jinping II hydropower station. Figure 1a shows a photograph of the sampling spot, which is located in the auxiliary tunnel. Specifically, the marble samples were processed by using the spalling blocks (about  $1000 \times 450 \times 80\text{mm}^3$ ) by rockburst as well as the pan burst pit formed at the site. X-ray diffraction (XRD) analysis results indicate that the major minerals in the marble samples are calcite (67.4%), dolomite (20.6%) and clay minerals (11.6%, mainly chlorite and illite). Figure 1b illustrates an SEM photo of dolomite crystal clusters on the surface



**Fig. 1** a Sampling site of the marble samples, b high resolution SEM images of dolomite crystals, and c flaky chlorite



of the marble sample. The crystal shape is evident, and the crystal bonding is tight. Figure 1c shows the microstructure of flaky chlorite. Besides the obvious lamellar structure, there have been also identified some micro-cracks. Additionally, three cylindrical marble specimens with nominal dimensions of 50 mm in diameter and 100 mm in length were prepared for uniaxial compression tests. The test results are presented in Table 1. The mean value of the uniaxial compression strength is 108.4 MPa. Additionally, Table 1 also presents the P-wave velocities of marble; specifically, the mean P-wave velocity is  $\sim 5584 \text{ m s}^{-1}$ . Young's modulus and Poisson's ratio are 54.9 GPa, and 0.24, respectively.

## 2.2 Experimental System

In this study, the *Deep Rock Nonlinear Mechanics Experimental System* (He et al. 2018) was used to perform rockburst tests. Figure 2a shows the experimental system. The main machine represents a true triaxial loading system and the loading capacity in all three directions is 500kN. The control system uses a controller manufactured by the NI company. Additionally, the main machine can apply about 12 types of disturbance loads (sine wave, triangular wave, square wave, etc.) and the loading frequency ranges from  $10^{-6}$  to 10 Hz. Moreover, the experimental system contains supplementary monitoring systems, such as the AE system and a high-speed image recording system.

**Table 1** Physical and mechanical properties of the marble

Density ( $\text{g/cm}^3$ )	Mineral components (%)			P-Wave velocity (m/s)	UCS (MPa)	Young's modulus (GPa)	Poisson's ratio
	Calcite	Dolomite	Clay				
2.80	67.4	20.6	11.6	5584	108.4	54.9	0.24

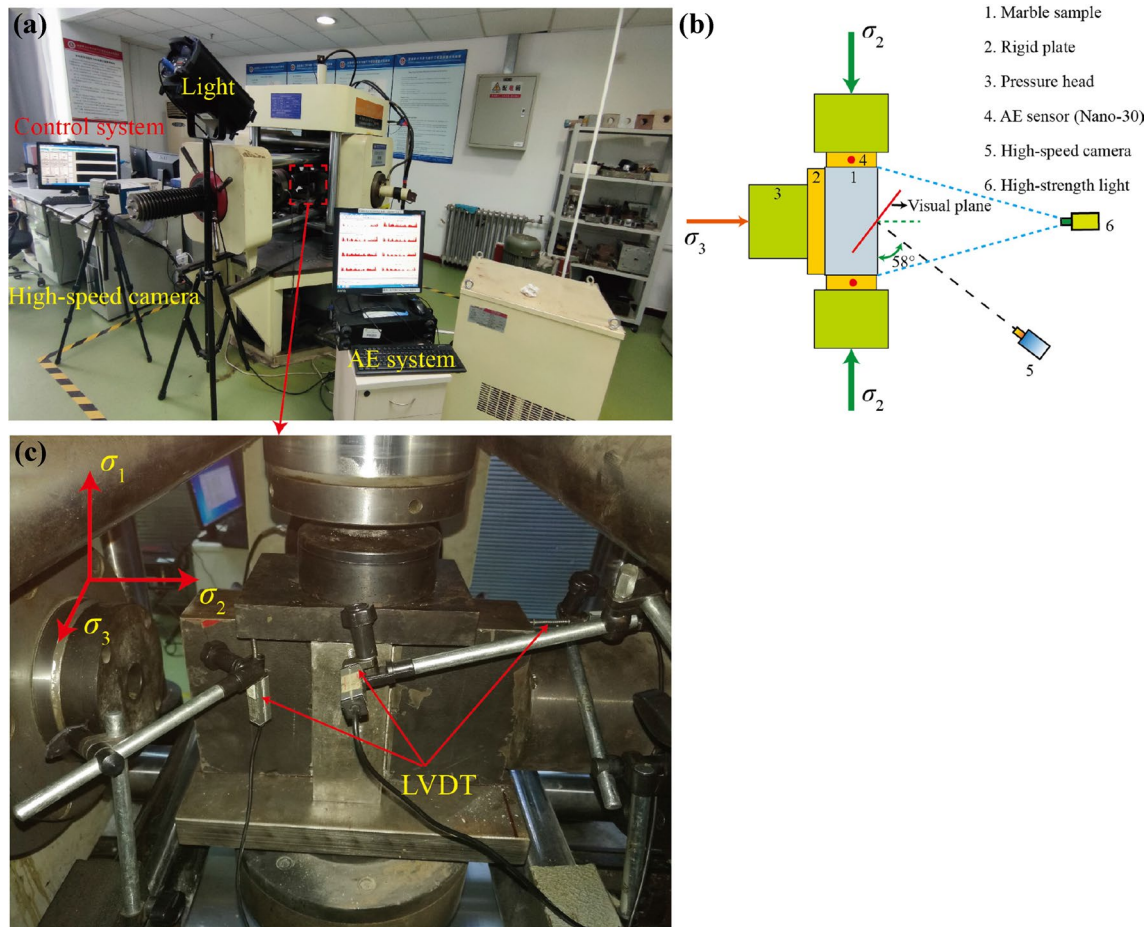


**Fig. 2** a Experimental and monitoring system, b top view of the high-speed camera position, and c arrangement of the LVDT

AE monitoring was carried out by using a PIC-2 system produced by the American Physical Acoustics Corporation. In this study, the AE signals were amplified by 100 times (amplifier was set to 40 dB); and the threshold, the sampling frequency, and the sampling length were set to 45 dB, 2 MHz, and 4096 data points, respectively. Two Nano-30 sensors with a response frequency of 100–400 kHz were operated to acquire the AE signals. The sensors were glued to the loading plate as shown in Fig. 2b. It has been demonstrated that the amplitude of the signals, as well as the variation trend, is completely consistent when the AE sensor is located on the specimen or the loading plate (Su et al. 2017b). Figure 2b also shows the specific location of the high-speed camera and illustrates that the angle between the camera axis and the intermediate principal stress axis is  $\sim 58^\circ$ , while the distance between the camera and the specimen is 859 mm. Additionally, high-strength light emission from an auxiliary device ensured smooth recording of the high-speed shooting process. Figure 2c highlights the arrangement of the LVDT to measure high precision displacements in three directions.

### 2.3 Experimental Design

During construction operations of deep-buried tunnels in high-stress areas, it is often required to excavate an auxiliary parallel tunnel that is ahead of the main tunnel (Fig. 3a). For the surrounding rock elements of the tunnel, there have been detected three typical stress transformation processes. Rock element 1 is primarily affected by excavation unloading and tangential stress concentration. If rockburst occurs, then it is driven by static stress concentration. Additionally, the occurrence of rockburst can be simulated by the loading stress path shown in Fig. 3. Specifically, the three-direction principal stresses are first loaded to the initial in situ stress level ( $\sigma_{10}/\sigma_{20}/\sigma_{30} = 35.4 \text{ MPa}/22.5 \text{ MPa}/14.5 \text{ MPa}$ ), the  $\sigma_3$  is unloaded to simulate the excavation unloading effect, and then the  $\sigma_1$  is uniformly loaded until the rockburst occurs.

However, rock elements 2 and 3 are affected by the same excavation unloading and tangential stress concentration parameters; however, the stress concentration does not reach the rock failure strength, while the rockburst can be triggered by different types of dynamic disturbances. In the case of

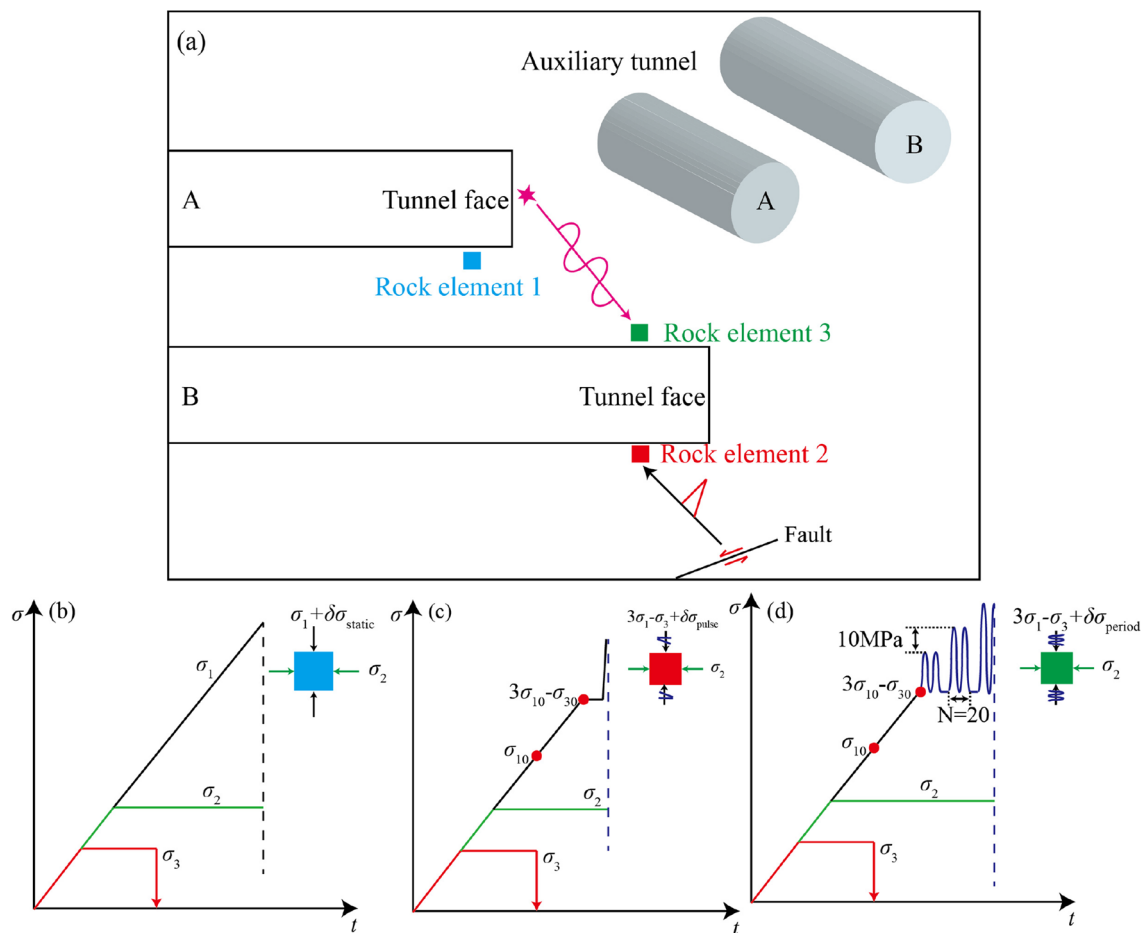


Fig. 3 a Schematic of the typical rock element of the surrounding rock, b–d loading paths of three types rockburst, respectively

element 2, the PUDR is caused by the disturbance of the pulse load (such as fault dislocation). The loading stress path is illustrated in Fig. 3c. After unloading  $\sigma_3$ ,  $\sigma_1$  is uniformly loaded to  $3\sigma_{10}-\sigma_{30}$ , and then  $\sigma_1$  is increased to rockburst at the fastest loading rate (10 times the initial loading rate, the maximum of the test system). Moreover, compared with element 2, element 3 is predominantly exposed to the periodic dynamic disturbance of the delayed excavation tunnel (such as the mechanical disturbance). The loading stress path is shown in Fig. 3d. When  $\sigma_1$  increases to  $3\sigma_{10}-\sigma_{30}$ , the sinusoidal load is used to simulate the periodic disturbance. In this study, the sinusoidal disturbance with an incremental increase in amplitude was applied, while each amplitude level was disturbed 20 times. If there was no PEDR, then the amplitude was increased by 10 MPa (simulating the shortening of the distance between two tunnel faces) and then disturbed 20 times again until rockburst occurred.

## 2.4 Multifractal Spectrum

Multifractal theory mainly describes the instability and inhomogeneity of things (Sayed et al. 2015; Tamás et al. 2005). The failure of rock is a nonlinear and complex process, and the AE signals are also nonlinear and discrete (Xu et al. 2011), because the AE signal mainly reflects the initiation and propagation of microcracks. Therefore, some scholars have applied multifractal to the study of AE characteristics during rock failure (Kong et al. 2016a; Liu et al. 2022; Zhang et al. 2015). In this paper, the AE characteristic of rockburst was analyzed based on the multifractal theory, which can effectively reveal the mechanism of rockburst.

In this paper, the box dimension method (Hu et al. 2014; Kong et al. 2019) was used to calculate the multifractal spectrum of the AE time series of different marble rockbursts. The time series is  $\{T_i\}$  which can be divided into  $N$  subsets with the length  $n$ , and the probability distribution of each subset was calculated as  $\{P_i(n)\}$ . If the time series satisfy multifractal characteristics, the probability distribution function and  $n$  ( $n \rightarrow 0$ ) satisfy the following formula (Zhang et al. 2020; Kong et al. 2017):

$$\{P_i(n)\} \sim n^\alpha \quad (1)$$

where, the singularity index  $\alpha$  is a constant, which mainly reflects the singularity of  $\{P_i(n)\}$  and shows the unevenness of the probability subset; if the number of units with the same probability in the  $\alpha$ -labeled subset is denoted as  $N_\alpha(n)$ , the smaller the division scale  $n$  is, the more subsets are obtained, and  $N_\alpha(n)$  decreases with the increase of  $n$ :

$$N_\alpha(n) \propto n^{-f(\alpha)} \quad (2)$$

where,  $f(\alpha)$  is the frequency of the subset represented by  $\alpha$  in the entire subsets, also known as the fractal dimension of

$\alpha$  subset. In the actual calculation process, it is difficult to calculate the fractal dimension according to the definition. At present, the multifractal spectrum is mainly calculated by the statistical physics method (Kong et al. 2016b; Li et al. 2018a, b). Firstly, define a partition function:

$$x_q(n) \equiv \sum p_i(n)^q n^{\tau(q)} \quad (3)$$

where,  $x_q(n)$  is the function that defines the assignment;  $\tau(q)$  is the quality index, which is a specific function of multifractality,  $-\infty < q < +\infty$ ,  $q$  is the weight factor, and the value of  $q$  represents the heterogeneity of multifractality (Zhang et al. 2018). In practical calculations, when  $|q|$  reaches a certain value, the multifractal spectrum tends to be stable. Therefore,  $q$  is usually limited to a certain range. The value of  $q$  in this paper is ranging from  $-20$  to  $20$ . When the defined distribution function has a power-exponential relationship with the division scale  $n$ , the value of  $\tau(q)$  can be calculated by the slope of the double logarithmic curve  $\ln x_q(n) - \ln n$ , that is:

$$\tau_q = \lim_{n \rightarrow 0} \frac{\ln x_q(n)}{\ln n} \quad (4)$$

By applying the Legendre transformation to Eq. (2), the relationship between  $\tau(q)$  and  $q$  can be expressed as:

$$\alpha = \frac{d(\tau(q))}{dq} = \frac{d}{dq} \left( \lim_{n \rightarrow 0} \frac{\ln x_q(n)}{\ln n} \right) \quad (5)$$

$$f(\alpha) = \alpha q - \tau(q) \quad (6)$$

The relationship curve of  $\alpha$ - $f(\alpha)$  is a multifractal spectrum of the calculated sequence which can reflect the inhomogeneity and the randomness of the signal. Larger multifractal spectrum width values ( $\Delta\alpha = \alpha_{\max} - \alpha_{\min}$ , the subsets of  $\alpha_{\max}$  and  $\alpha_{\min}$  represent the small and the large energy signals in the AE time series, respectively), generate more intense fluctuations of the signal distribution. The  $\Delta f(\alpha)$  ( $f(\alpha_{\max}) - f(\alpha_{\min})$ ) represents the frequency of different energy signals. Small  $\Delta f(\alpha)$  values indicate an increase in large energy signals, as well as a higher degree of rock fracture, and vice versa.

## 3 Results and Discussion

### 3.1 Stress–Strain Curves

As illustrated in Fig. 4a, the stress–strain curves in the  $\sigma_1$  direction of the three different types of rockbursts indicate a good consistency at the beginning of the loading stage and show differences after reaching  $3\sigma_{10}-\sigma_{30}$ . The stress–strain curve of the SDR continues to slightly increase after yielding. In the case of the PUDR, the stress–strain curve has

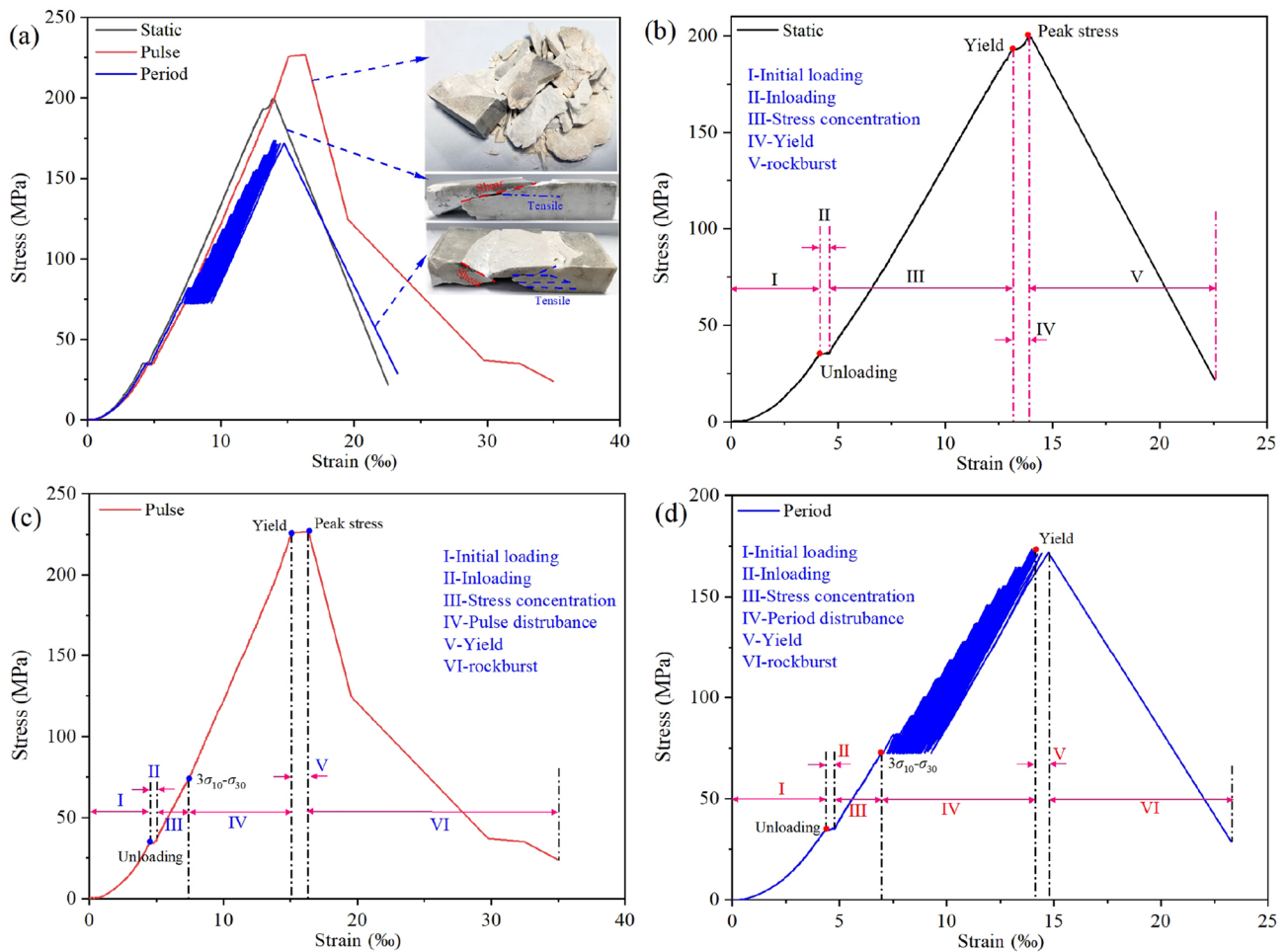


**Fig. 4** **a** Stress–strain curves (in the  $\sigma_1$  direction) of the three types rockburst and **b–d** division of the loading stages for the SDR, PUDR and PEDR, respectively

an obvious yield platform. The yield characteristics of the PEDR are not evident, and the stress slightly decreases after yielding. Table 2 lists the specific values of the yield stress, the rockburst stress, the residual stress ratio, the yield strain, and the maximum principal strain of the three types of rockburst. By combining with Fig. 4a and Table 2, it can be observed that the degree of difficulty in the occurrence of rockburst in marble for the three different loading methods is different. The stress of the PUDR has the highest values,

which means that the chances of this rockburst to occur are low, while the stress of the PEDR has the lowest values, which means that the chances of this rockburst to occur are high.

Although the PEDR is more likely to occur than the SDR, the strain value of the PEDR at the rockburst point is greater due to the influence of cyclic dynamic disturbance. However, the strain values of the previously mentioned two types of rockburst are smaller than those of the PUDR. Similarly, the

**Table 2** Failure information of the three types rockburst

Type	$\sigma_1$ of yield (MPa)	Failure stress ( $\sigma_1$ ) (MPa)	Residual stress (MPa)	Residual stress ratio <sup>a</sup>	Stress drop rate (MPa/s)	$\epsilon_1$ of yield (%)	Maximum $\epsilon_1$ (%)
SDR	193.03	199.59	21.86	0.110	443.9	13.10	22.52
PUDR	225.55	226.57	23.97	0.106	1904.8	15.11	34.98
PEDR	173.50	171.83	28.43	0.165	349.0	14.13	28.79

<sup>a</sup>Residual stress ratio is the ratio of residual stress to failure stress

yield strain and the maximum principal strain have the same regularity. Additionally, the stress drop characteristics of  $\sigma_1$  in the rockburst are distinct. The corresponding stress drop rate values are given in Table 2. For the PU DR, the stress drop rate is 4.3 and 5.5 times higher than the SDR and the PEDR values, respectively. Therefore, from the stress drop rate perspective, the PU DR and the PE DR have the strongest and the weakest intensities, respectively.

According to the stress–strain curve in the  $\sigma_1$  direction, the loading process of the three types of rockbursts can be divided into different loading stages, as illustrated in Fig. 4b–d. For all types of rockbursts, the first two stages are the initial loading stage (stage I) and the unloading stage (stage II). The curve of stage I is concave, indicating that there are noticeable compaction properties in the sample. While  $\sigma_1$  remains unchanged during the unloading stage, the strain slightly increases due to the Poisson effect of the free surface after the unloading of  $\sigma_3$ . The stress concentration stage (III) of the SDR (Fig. 4a) has evident elastic characteristics, and the specimen shows strain hardening properties after reaching the yield stress (stage IV). The modulus of the rockburst stage (V) is mostly the same as the loading modulus of stage III.

The division of the subsequent four stages is essentially the same for the stress–strain curves of the PU DR (Fig. 4b) and the PE DR (Fig. 4c), with prominent differences in the loadings of stage IV. For the PU DR, the elastic modulus values of the pulse loading stage (IV) are slightly greater than the values of the static stress concentration stage (III). There is a short yield platform after reaching the yield stress, and the peak stress is approximately equal to the yield stress. The rockburst stage shows the typical characteristics of piecewise drop. Specifically, the first stage is the most obvious, and the subsequent unloading modulus gradually decreases.

However, for the PE DR, the difference between the loading and unloading elastic modulus in the periodic disturbance stage and the elastic modulus in the static stress concentration stage is small. When the disturbance amplitude reaches a high level, evident plastic characteristics can be noticed. After reaching the yield stress, the strain increases significantly, and rockburst occurs at the stress below the yield stress. Moreover, the unloading modulus in the rockburst stage is consistent with the loading elastic modulus in stage IV.

### 3.2 Energy Consumption and Failure Mode

#### 3.2.1 Energy Consumption

Figure 5A illustrates the diagram of the strain energy calculation in the  $\sigma_1$  direction. If the PE DR is considered as an example for illustrating the calculation process of the strain energy, then the total strain energy can be divided into four parts, as shown in Eq. (5). During the cyclic disturbance stage of the PE DR, there is energy input and release in each loading and unloading process. To simplify the calculation process, this study measures the energy input derived from the final deformation caused by each level of the disturbance load. Specifically, the total strain energy is calculated by the outer envelope of the stress–strain curve during this stage. The elastic strain energy ( $U_e$ ) accumulated during the early stage of rockburst is suddenly released and partially converted into the kinetic energy of the ejection fragments.  $U_e$  is the area of the triangle (Fig. 5a), and the slope of the diagonal line of the triangle represents the loading elastic modulus. The dissipation energy ( $U_{d1}$ ) before rockburst is the difference between the total strain energy ( $U$ ) before rockburst and

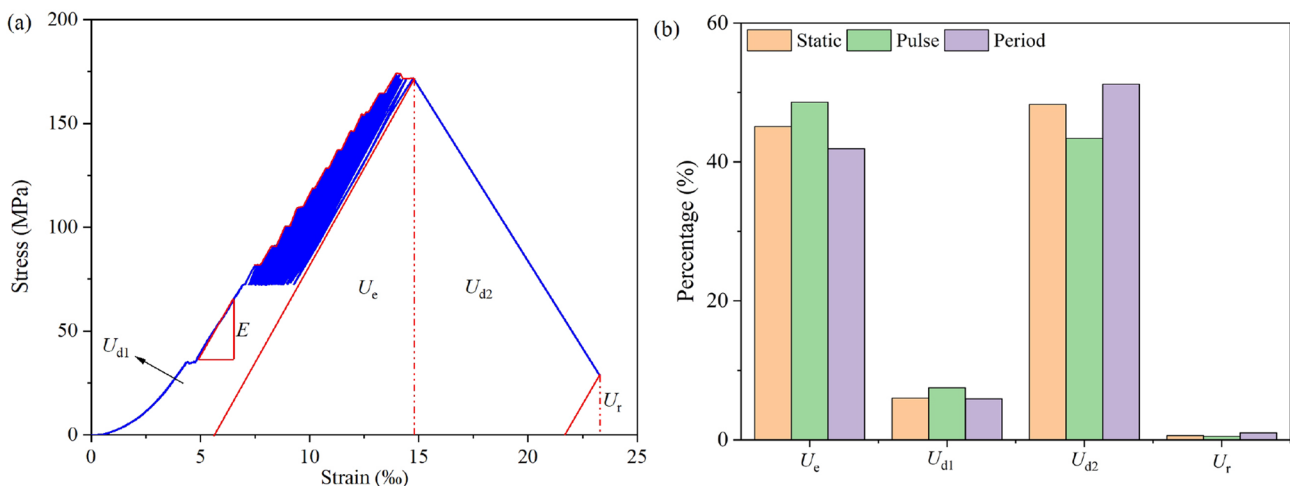


Fig. 5 a Schematic of strain energy density calculation and b percentage of the different strain energies from the total energy



$U_e$ . During the rockburst stage, the propagation, and the coalescence of microcracks will lead to energy dissipation ( $U_{d2}$ ), and eventually, the residual strain energy ( $U_r$ ) will keep inside the parent rock.

$$U = U_{d1} + U_e + U_{d2} + U_r \tag{7}$$

where,  $U$  is the total strain energy;  $U_{d1}$  and  $U_{d2}$  represent the dissipation energy before and during rockburst, respectively;  $U_e$  and  $U_r$  are the elasticity and residual strain energy, respectively.

Figure 5b is a bar chart that illustrates the proportion of each type of energy from the total strain energy for the three types of rockbursts. The specific numerical details are listed in Table 3. The proportions of  $U_r$  for the different types of rockbursts are small, and the maximum value is only 1.0%. The energy ( $U_{d1}$ ) consumed by plastic deformation before rockburst is less than 8%, and the proportions of  $U_e$  and  $U_{d2}$  are more than 40%. Specifically, the PUDR accumulates the most  $U_e$  before rockburst, but the dissipated energy during rockburst is the least. In contrast, the PEDR accumulates the least amount of energy before rockburst and consumes the most amount of energy during rockburst. Therefore, from the energy viewpoint, the PUDR has the highest intensity, while the PEDR has the smallest.

### 3.2.2 Failure Mode

As shown in Fig. 4a, failure during the PUDR is the most severe and is characterized by the disintegration of the sample into blocks. However, the SDR and the PEDR samples still have relatively unbroken parent rocks after failure. Additionally, distinct shear and tension cracks can be observed on the surface of the intermediate principal stress direction of the specimen. For the SDR, the penetrating shear crack intersects the free surface at  $12^\circ$ , while the tensile crack is approximately parallel to the free surface. However, the free surface of the PEDR specimen has an obvious concave burst pit, and the splitting blocks are represented by flakes. There are several tensile cracks parallel

to the free surface, while the intersection angle between the shear crack and the free surface is about  $45^\circ$ . Therefore, the application of cyclic disturbance load causes the marble to display buckling cracks and bending failure.

Figure 6 illustrates high-speed images of the ejection failure process for the three types of rockburst. For the SDR and the PUDR, there are severe ejection phenomena, while the PEDR has obvious splitting and spalling phenomena, accompanied by a relatively weak ejection. The rockburst process of the PEDR has the longest duration (1356 ms), which is about 12 times and 2 times greater than the SDR duration (116 ms) and the PUDR duration (680 ms), respectively. Before the three types of rockbursts occur, there are transverse cracks on the free surface. Failure of the SDR and the PUDR happens suddenly in both instances, and the intensity ejection occurs in the middle and lower parts of the sample. Additionally, the PUDR also displays local ejection in the upper part of the sample. The ejection processes of the SDR and the PUDR are also mostly similar. In the beginning, there are both horizontal and oblique (downward) ejections. However, with the development of the ejection process, the ejection is affected by the interaction between the subsequently ejected fragments, which causes some fragments to be ejected with an oblique upward direction. The angles of the oblique upward and downward ejected fragments of the SDR and the PUDR are mostly the same, both close to  $90^\circ$ . Moreover, distinct burst pits appear on the free surface after the ejection process, and the burst pit depth of the SDR is deeper than the one created by the PUDR. Compared to the SDR and the PUDR, the PEDR has evident characteristics typical for the evolution of rockburst: cracking, ejection, bending, spalling, and bursting, and a burst pit area with the largest surface.

By screening the ejected or the broken fragments collected from the different types of rockbursts, the mass distribution of the fragments with different particle sizes was calculated as shown in Fig. 7. The proportion of coarse fragments with particle sizes greater than 10 mm represents more than 60%, while the proportion of fragments with particle sizes smaller than 10 mm is less than 20%. For the PUDR, the mass percentage of coarse fragments has the lowest value (67%), while the mass percentage of the smaller fragments (smaller than 10 mm) has the highest values when compared to the other types of rockburst. This suggests that the fragmentation of the ejected fragments is less intense. On the contrary, for the PEDR, coarse fragments accounted for more than 90%, indicating that the break of fragments generated by splitting under cyclic disturbance load is more intense.

**Table 3** Strain energy density of the three types rockburst in the  $\sigma_1$  direction

Type	Total energy density (mJ/mm <sup>3</sup> )	Percentage of parts to total strain energy (%)			
		$U_e$	$U_{d1}$	$U_{d2}$	$U_r$
SDR	2.14	45.1	6.0	48.3	0.6
PUDR	3.17	48.6	7.5	43.4	0.5
PEDR	2.03	41.9	5.9	51.2	1.0

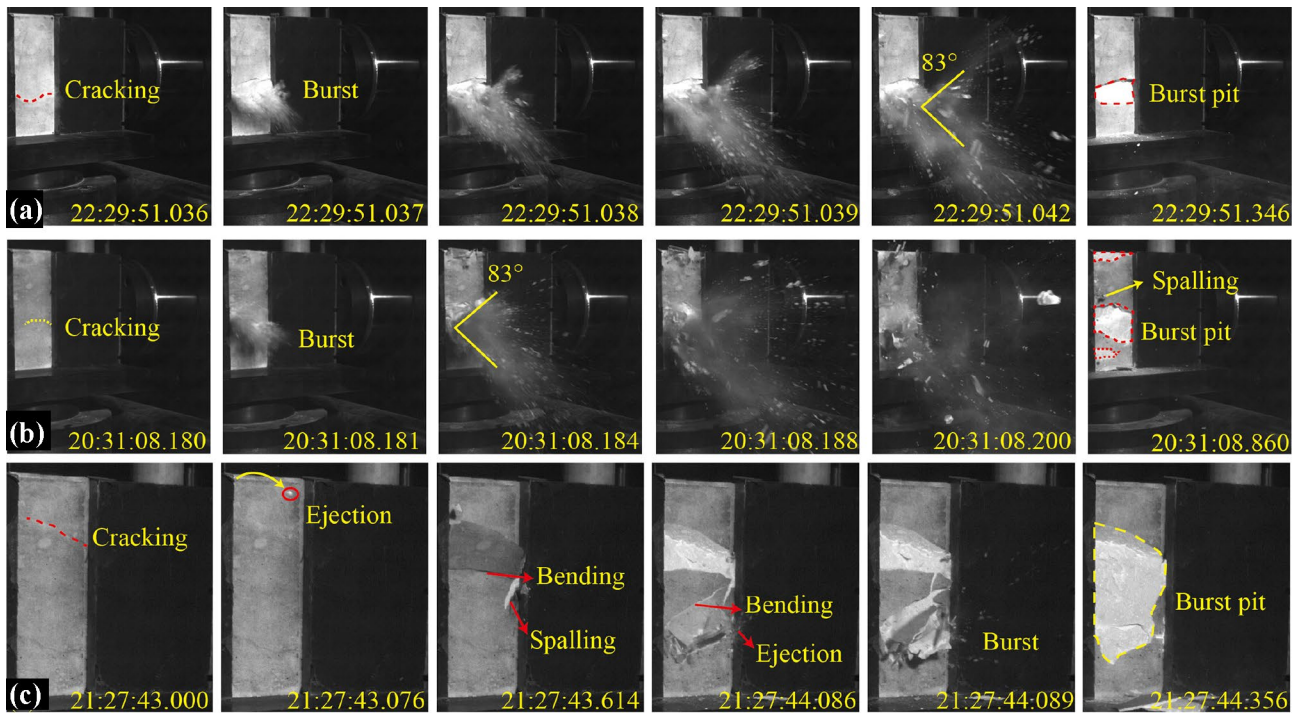


Fig. 6 Ejection processes of rockburst; a–c for the SDR, PUDR and PEDR, respectively

### 3.3 Ejection Velocity Field

The particle image velocimetry (PIV) method was used to analyze the high-speed images of the ejection failure process. In this case, the horizontal velocity of the ejection process was corrected based on the shooting angle. Figure 8 shows the average velocity variation curve of the free surface and the velocity vector field at typical points for the three types of rockbursts. For the SDR, the average velocity of the

free surface sharply increases at the initial ejection, and suddenly decreases just as the fragments are discharged. When the fragments are completely separated from the parent rock, a small number of coarse-sized fragments fall freely, which causes the average velocity of the free surface to increase again and subsequently decay to zero.

It can be seen from the velocity vector field that during the initial ejection the free surface in the middle and upper parts of the sample shows obvious protrusion phenomena. However, the ejection only occurs in the fracture area of the middle and lower parts of the sample. There is a factor of extrusion convergence in the area where surface cracks appear. Additionally, the velocity vector direction of the front edge of the ejected fragments is mainly horizontal to the right and oblique to the bottom, with a maximum horizontal initial velocity equal to 8.68 m/s. Afterwards, with the development of the ejection process, the maximum horizontal ejection velocity initially increases and then decreases, reaching a maximum value of 16.74 m/s. The main reason for the increase is the forward thrust of the subsequently ejected fragments. After the interaction between the front and the rear fragments, the ejection direction of the fragments positioned behind is deflected (from horizontal forward to oblique upward). Moreover, the fragments at the front edge rebound after encountering obstacles and collide with the fragments at the rear edge, resulting in the cross-aggregation or divergence of velocity vectors at similar locations.

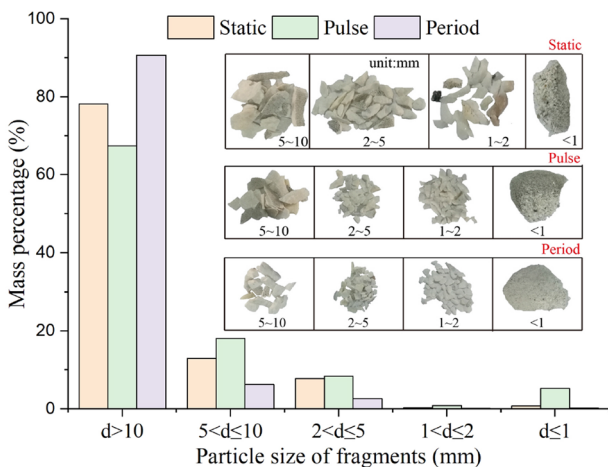


Fig. 7 The distribution of mass percentage content and the corresponding photos of the ejected fragments

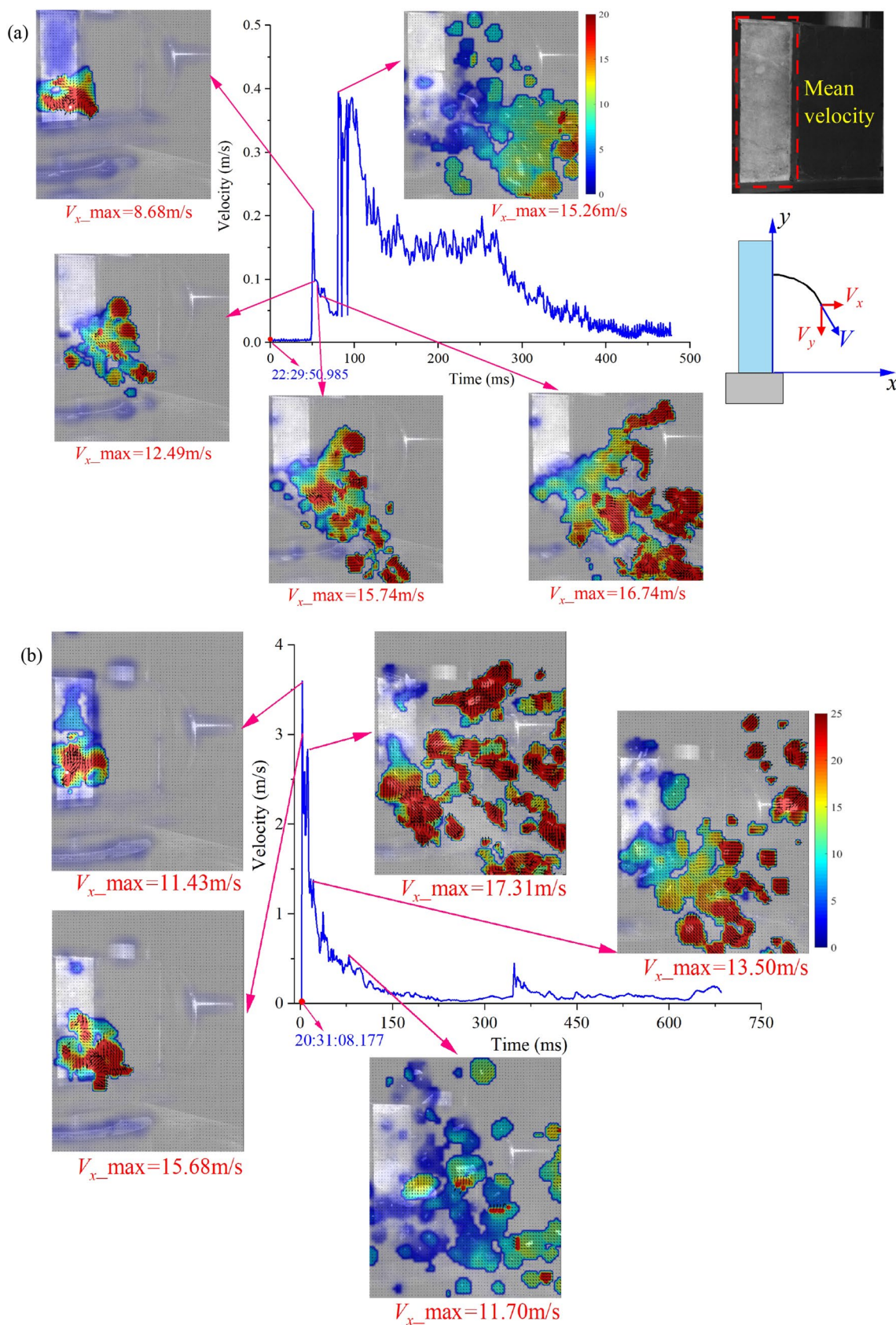


Fig. 8 Variation of the velocity fields for the marble free faces during rockburst, a–c respectively for the SDR, the PUDR and the PEDR



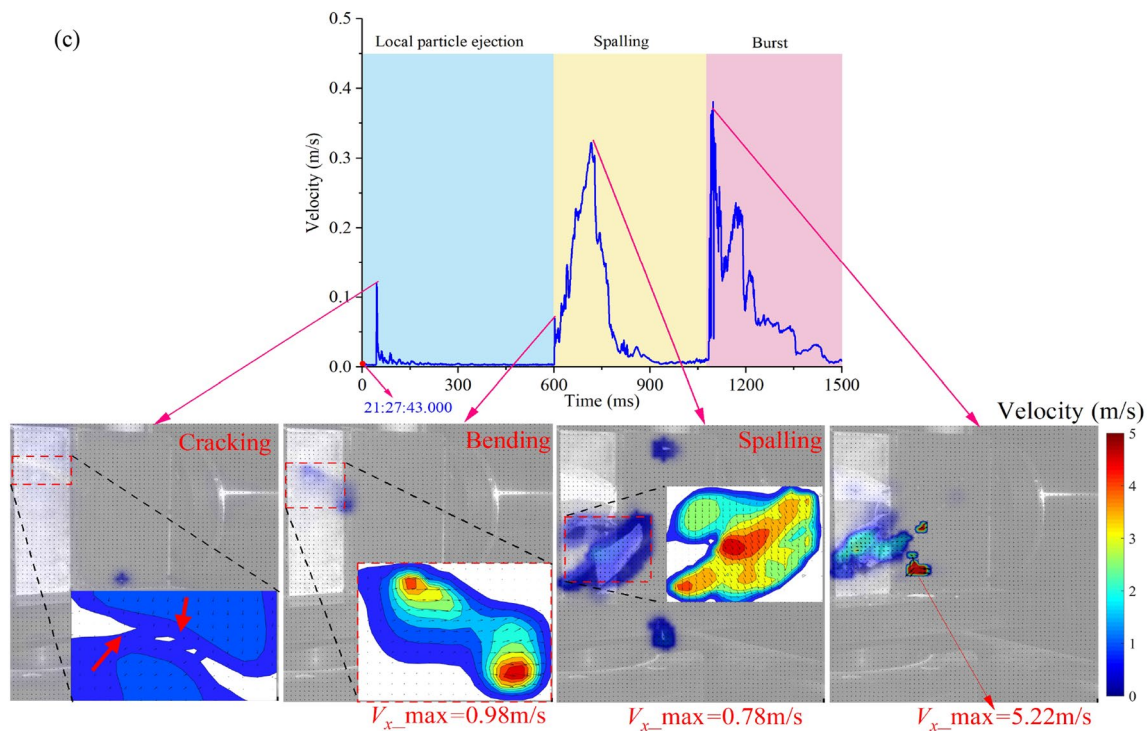


Fig. 8 (continued)

In the case of the PUDR, the average velocity variation of the free surface is similar to that of the SDR, but its average velocity is about 9 times greater. Also, the average velocity of the free surface reaches its peak at the initial ejection, and then quickly declines. The initial horizontal velocity is 11.43 m/s (1.32 times greater than that of the SDR), and the maximum value reaches 17.31 m/s, which is first increasing and then decreasing. The velocity vector field shows that the velocity vector at the initial ejection is mainly inclined upward, which indicates that the reaction force in the lower part of the sample is more evident, resulting in the formation of free surface cracks. Additionally, during the early stage of ejection, the interaction between fragments is obvious. The upper fragments are thrown down obliquely, while the lower fragments are thrown up obliquely. After progressing into the middle stage of the ejection process, the collision between fragments is strengthened further. This produces the obvious scattering characteristics of the velocity vector field, while the velocity vectors in the local area are intertwined. However, during the following stage of ejection, the interaction is gradually weakened, the continuity of the vector field is enhanced, and the motion direction is mostly constant.

In comparison with the SDR and the PUDR, the average velocity evolution of the PEDR can be divided into three stages: local particle ejection, spalling and burst stages. The cracking, bending, and spalling processes correspond to the maximum peaks of the average velocity. When cracks appear

on the surface of the sample, an obvious mutual extrusion phenomenon can be seen on both sides of the crack, and the velocity vector has an approximately opposite direction. Additionally, when bending occurs, the velocity vector direction in the fracture area is horizontal to the right, and the maximum horizontal velocity is only 0.98 m/s. Afterwards, the velocity vector of the surface spalling block has an oblique downward direction, and when the severe ejection occurs, the maximum horizontal velocity reaches 5.22 m/s. Therefore, from the perspective of the initial ejection velocity, the rockburst intensities of the PUDR, the SDR and the PEDR decrease successively.

### 3.4 Characteristics of AE

#### 3.4.1 Parameters Characteristics

Figure 9 illustrates the variation of AE count rates and energy rates plotted on the stress-time Axes. For the three different types of rockbursts, the evolution process of the AE count rates (the parameter of AE activity) and the energy rates is similar. During the initial loading stage the AE activity is low. The AE activity is temporarily strengthened when unloading the minimum principal stress, but the enhanced AE signals release less energy because the energy rate does not change significantly. Additionally, during the continuous variation stage of  $\sigma_1$ , the activity of the AE maintains at a



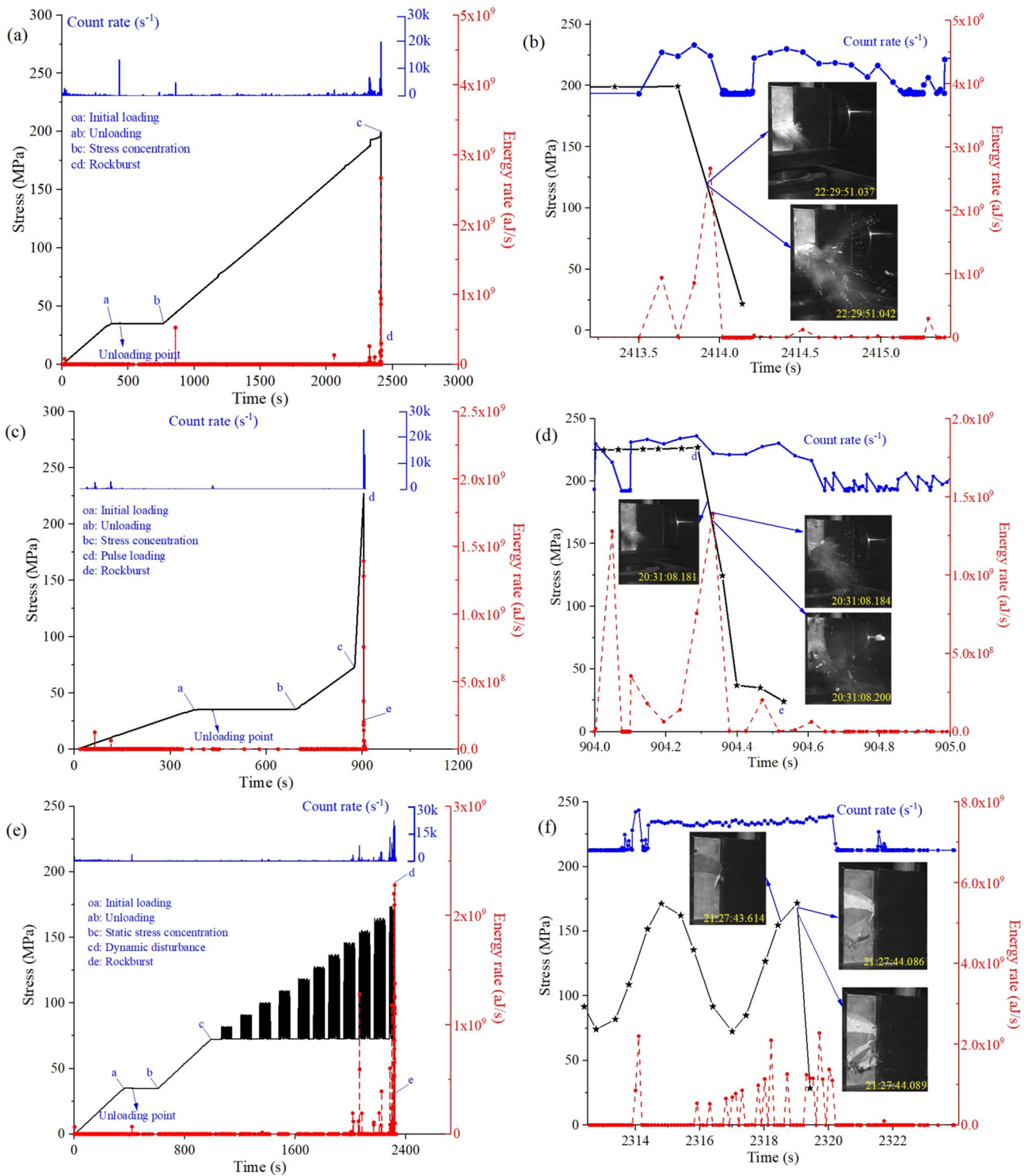


**Fig. 9** Variations of AE counts rate and energy rate with loading path; **a–b**, **c–d** and **e–f** respectively for SDR, PU DR and PE DR

low level over a long period. However, the AE shows strong activity close to and during the rockburst stage, accompanied by a large and dense energy release. For the SDR and the PE DR, the AE count rate has a distinct quiet period before

rockburst, which means that more micro-cracks enter the quiet period, until the uprush of the AE signals during the rockburst stage. In contrast, the PU DR doesn't have a distinguishable quiet period. Moreover, as far as energy release

characteristics are concerned, the intense energy release of the SDR and the PUDR occurs only during the rockburst stage, while the PEDR also shows a relatively strong energy release during the application of the 9th and 10th cyclic disturbance loads. This indicates that the application of the previously mentioned disturbance loads has produced more micro-cracks in the specimen.

By incorporating the ejection failure phenomenon of the three types of rockbursts, it can be observed that the severe ejection failure of the SDR and the PUDR occurs during the process of stress decline, which corresponds to the process of energy release, and the sudden increase of the AE count is ahead of the ejection failure phenomenon (Fig. 9b, d, and f). However, the AE count rate fluctuates during the rockburst stage, which makes it difficult to accurately calculate the corresponding relationship between the sudden increase of the AE count rate and the rockburst. Therefore, it is less practical to use the activity parameters of AE signals alone as the precursor of rockburst. For the PUDR, there is a short intermittent period between the two intensity energy releases. The AE count rate during the intermittent period maintains a high value, indicating that dense but less energetic micro-cracks appear in the specimen before the intensity ejection. However, for the PEDR, the ejection of fragments and the splitting of blocks appear before the peak load, which implies that the stress of the specimen after the local fragment ejection and the spalling further increases. Consequently, this leads to the final relatively strong ejection, with the final ejection failure happening during the stress drop. Moreover, during the loading process of the last two sinusoidal perturbation waves, the AE activity maintains at a relatively active level with an intermittent energy release.

### 3.4.2 Multifractal Characteristics

Figure 10 illustrates the multifractal spectrum curves of the AE counts for the three types of rockbursts. The overall shapes of the multifractal spectra are analogous, where  $\Delta f(\alpha)$  initially increases and then decreases with the increase of  $\Delta\alpha$ , indicating that the failure processes of the different types of rockbursts are similar. However, the widths of the multifractal spectrum are different, suggesting that the microscopic fracture characteristics are distinct. In this case,  $\Delta(\alpha)$  values of the PUDR (1.63), the SDR (1.51) and the PEDR (0.83) decrease successively, while  $\Delta f(\alpha)$  values of the PEDR (1.20) and the SDR (1.01) have the maximum and minimum values, respectively. It can be observed from the physical meaning of  $\Delta\alpha$  and  $\Delta f(\alpha)$  in Sect. 2.4, that the AE signals fluctuation of the PUDR is the most violent, while the number of AE signals of the SDR with high energy values is the most numerous, corresponding to the highest rupture degree of the specimen. On the contrary, due to the

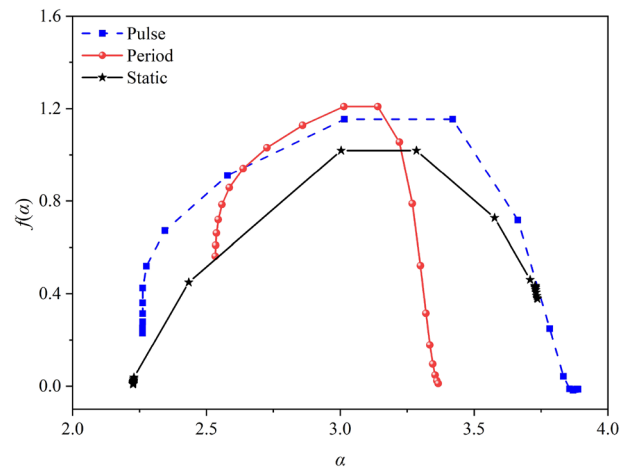


Fig. 10 Multifractal spectrum for the different types of marble rockburst

periodic disturbance load, the AE signals of the PEDR have a weak fluctuation, and the number of AE signals with high energy values is small, corresponding to the low rupture degree.

Figure 11 shows the variations of the multifractal parameters ( $\Delta\alpha$  and  $\Delta f(\alpha)$ ) of the three types of rockbursts plotted on the stress-time Axes. Overall, during the initial loading stage, the multifractal parameters greatly fluctuate. During the unloading stage, all the types of rockbursts display a decrease in  $\Delta\alpha$  and a sudden increase in  $\Delta f(\alpha)$ . In the case of the PUDR, the variation of  $\Delta\alpha$  is insignificant. After unloading the  $\sigma_3$ , the  $\Delta\alpha$  and  $\Delta f(\alpha)$  of the different types of rockburst show considerable variations. For the SDR,  $\Delta\alpha$  shows a general downward trend, specifically, the decrease line has the shape of steps during the static stress concentration stage. Additionally, a sudden drop (the decrement is about 20%) in  $\Delta\alpha$  occurs before rockburst, which is followed by a minor rebound (the increment is only 1.4%). However, the variation process of  $\Delta f(\alpha)$  is exactly the opposite of the  $\Delta\alpha$ , where the sudden increment before rockburst is also 20%, and a decrease of only 2.6% when rockburst occurs.

In addition, for the PUDR, the changes of  $\Delta\alpha$  and  $\Delta f(\alpha)$  during the stress concentration stage and the pulse disturbance stage are insignificant, and there is a slight downward and upward trend only during the stress concentration stage. When the rockburst stage is forthcoming,  $\Delta\alpha$  and  $\Delta f(\alpha)$  indicate a sudden decrease (34%) and increase (16%), respectively. When the rockburst occurs, a sudden increase (91%) and decrease (10%) is registered, respectively. Therefore, for the SDR and the PUDR, the fluctuation of the AE signal before rockburst sharply decreases, and the number of high energy AE signals decreases significantly. When rockburst occurs, the fluctuation of the AE signal is strengthened, and the number of high energy AE signals starts to

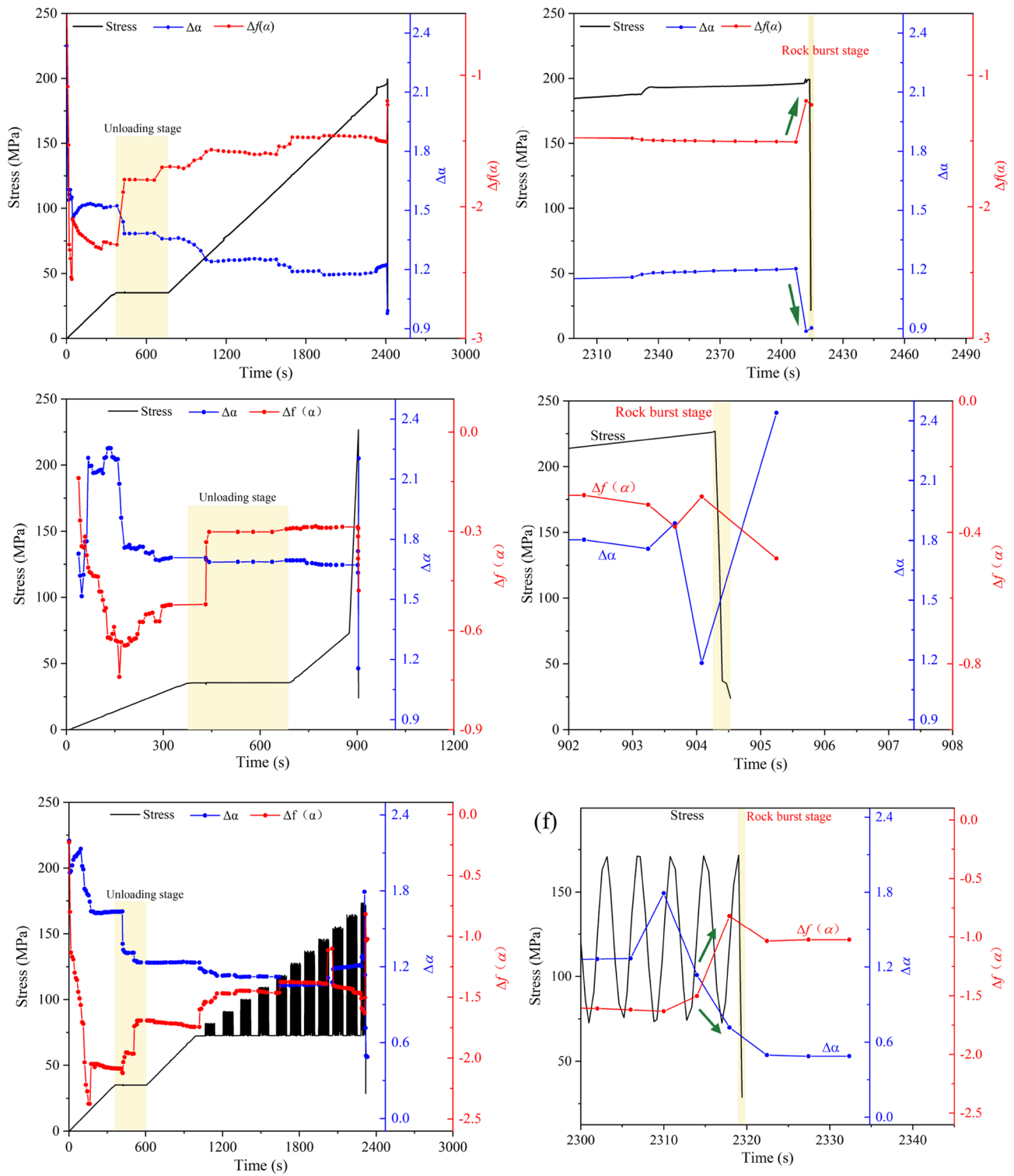


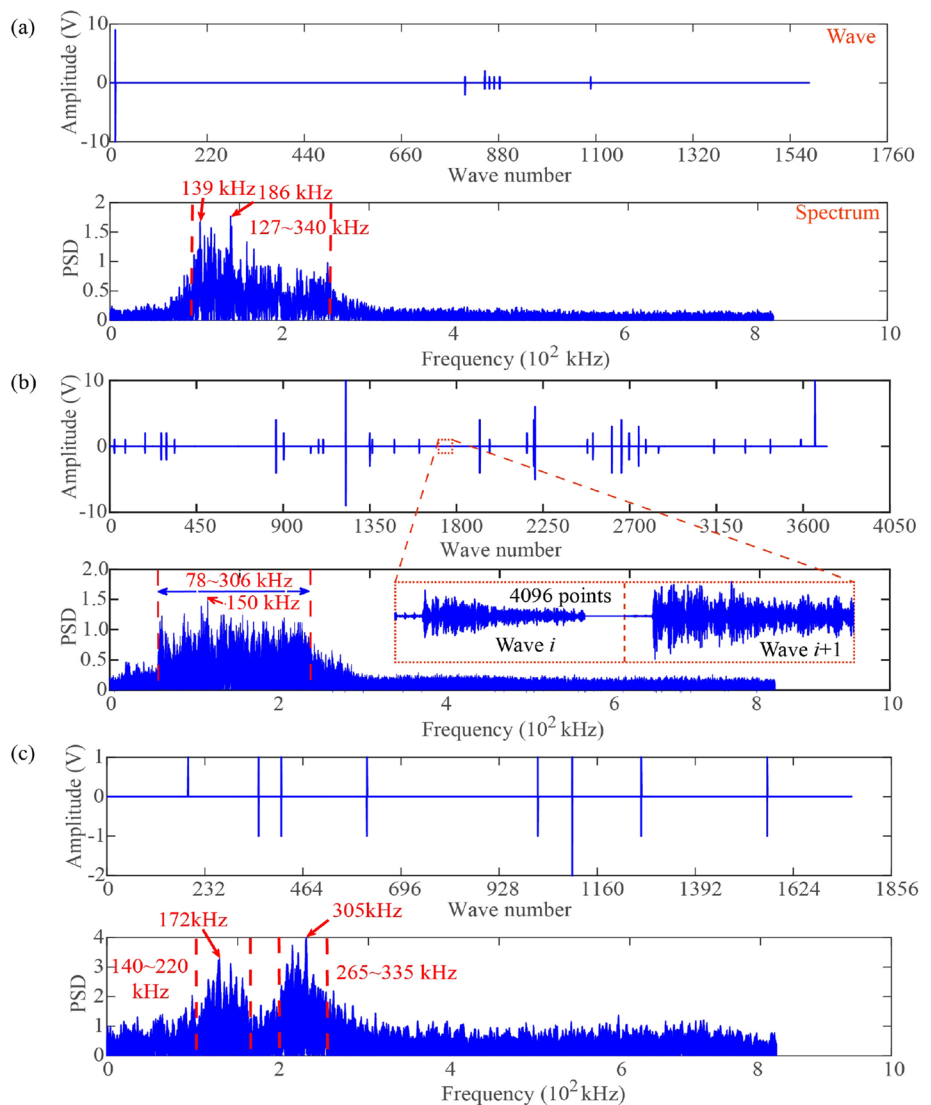
Fig. 11 The variation of multifractal parameters with loading path; a–b, c–d and e–f for the SDR, the PUDR and the PEDR, respectively

increase. In comparison, the fluctuation characteristics of the AE signals for the PUDR are more distinct, higher energy AE signals are generated, which corresponds to the greater rockburst intensity values. For the PEDR, the variation of the multifractal parameters during the period disturbance stage is relatively violent, especially after the 5th and 8th cyclic loads. Before and during rockburst,  $\Delta\alpha$  continues to decrease to a low level and then remains constant, while  $\Delta f(\alpha)$  initially increases and then decreases and finally remains stable. That is, before and during the rockburst of the PEDR, the volatility of the AE signals has been in an increasing variation process. Therefore, for the three different types of rockbursts, the number of high energy AE signals first decreases and afterwards increases before and during the rockburst, respectively.

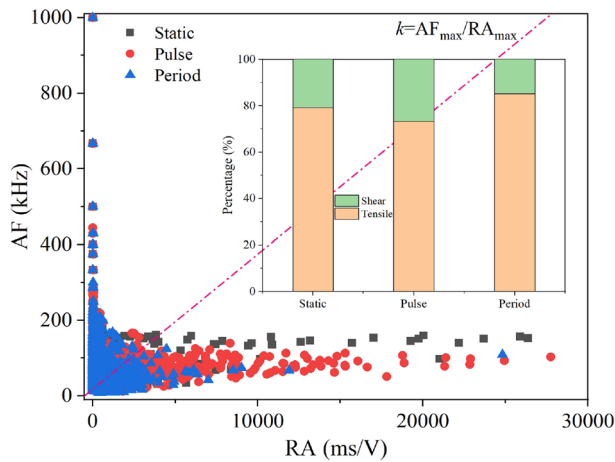
### 3.4.3 AE Waveform Characteristics

Figure 12 illustrates the waveform and the corresponding spectra of the AE waveform recorded during the rockburst stage. The waveform is obtained by the first and the last connection of each micro-crack waveform according to the sequence of occurrence (Fig. 12b). Regarding the number of waveforms, the PUDR has the greatest number of waveforms, and the SDR numbers are closer to the PEDR ones. The amplitude (voltage) of the PEDR waveform signal is the lowest, and the maximum value is one-tenth of the SDR and the PUDR. For the SDR, high amplitude signals are primarily concentrated at the beginning and the middle of the rockburst, while the PUDR is more frequent occurrence during the whole rockburst process. From the two-dimensional spectra of the AE waveform,

**Fig. 12** The AE waveform and corresponding spectrogram during the marble rockburst stage, a–c for the SDR, the PUDR and the PEDR, respectively







**Fig. 13** Crack type classification for micro-cracks occurred during the rockburst stage

the main frequency bands of the SDR (127–340 kHz) and the PUDR (78–306 kHz) have a single-segment distribution, while the PEDR indicates two main frequency bands (144–220 kHz and 265–335 kHz). According to the physical meaning of frequency (low and high frequency represent large- and small-scale micro-cracks, respectively), the micro-crack scale of the PUDR is relatively large, followed by the SDR, and the PEDR, respectively. Moreover, the PUDR micro-crack signals are mostly uniformly distributed throughout the entire frequency band, the SDR ones are mainly distributed in the left half of the main frequency band, while the PEDR micro-crack signals are distributed in two proximal frequency bands.

### 3.5 Micro-Cracking Mechanism and the Evolution of Stress

To further analyze the characteristics of tensile and shear micro-cracks during the rockburst stage, the average frequency and the RA (ratio of rising time to amplitude) of the three types of rockbursts were calculated. The corresponding relationship is illustrated in Fig. 13. The slope ( $k$ ) of the straight line plotted on the AF-RA coordinate system can be used to distinguish between the tensile and the shear micro-cracks (the tensile and the shear micro-cracks are positioned above and below the straight line, respectively). In this study,  $k$  was calculated as the ratio between the maximum values of AF and RA (Yue et al. 2020). Additionally, Fig. 13 also indicates the percentages of shear and tensile micro-cracks of the three types of rockbursts. Overall, the rockburst stage is dominated by tensile micro-cracks, accounting for more than

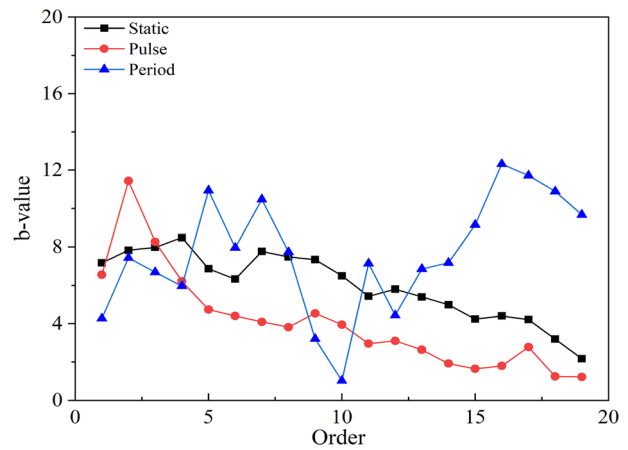


**Fig. 14** Variation of  $b$ -values of the AE signals occurring during the rockburst stage

70%. The proportion of shear micro-cracks in the PUDR, the SDR and the PEDR decreases successively, indicating that rapid loading (in the  $\sigma_1$  direction) will strengthen the shear effect, while period disturbance aggravates the rock damage and weakens the shear effect.

Figure 14 illustrates the evolution process of  $b$ -values corresponding to the AE signals generated during the rockburst stage. Due to the distinct number of waveforms for the different types of rockbursts, 20 values (that is, the waveform is divided into 20 sections) are selected to facilitate the presentation of the  $b$ -values' evolution process. Additionally, previous studies (Schorlemmer et al. 2005) have shown that the  $b$ -value can be used to represent the internal stress variations (or stress difference) in the rock. The size of the  $b$ -value is inversely proportional to the stress, which means that the increase and the decrease of  $b$ -values represent the release and the concentration of stress, respectively. It can be seen from Fig. 14 that the  $b$ -values of the SDR and the PUDR indicate a general downward trend, but slightly increase during the initial period of the rockburst. Additionally, the PUDR  $b$ -values are smaller, while the PEDR  $b$ -values show a fluctuating variation process. Therefore, for the SDR and the PUDR, the stress of the specimen was released when ejection occurred, and gradually concentrated with the development of the ejection process. The overall stress concentration trend was still accompanied by the stress release of individual periods. Moreover, for the PEDR, stress release and concentration appear alternately, which is related to the ejection of small particles on the free surface, the splitting and spalling of fragments, and the overall burst. All these characteristics correspond to the stress release.

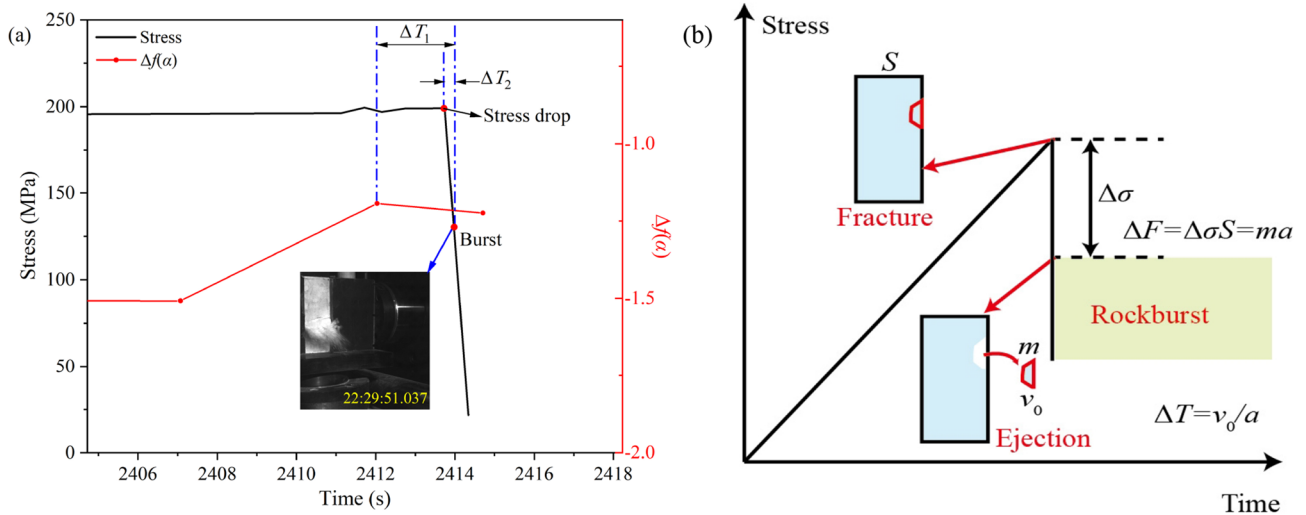


Fig. 15 a Schematic of the early warning time calculation, and b diagram of initial velocity source of the rockburst fragment

Table 4 Early warning times of three types rockburst

Type	Early warning time (s)	
	$\Delta T_1$	$\Delta T_2$
SDR	1.14	0.02
PUDR	0.24	0.03
PEDR	1.88	0.18

### 3.6 Early Warning Time

As discussed in Sect. 3.3.2, the multifractal parameter  $\Delta f(\alpha)$  increase and subsequent decrease can be used as the precursor feature of the rockburst, while the inflection point of increase and decrease can be accepted as early warning signals to calculate the early warning time  $\Delta T_1$  (Fig. 15a). Additionally, the stress drop can also be used as the precursor of rockburst. In the existing literature (Lou et al. 2019), the stress drop is regarded as a precursor index of rock mass instability which has been confirmed in the field of seismology and landslides. Rockburst occurrence in the surrounding rock mass needs to satisfy the following two conditions (Fig. 15b): the first one needs to meet the stress condition, that is, the stress value reaches the strength of the rock (the point after the peak); the second one needs to meet the velocity condition. When the first condition is satisfied, the failure of the surrounding rock generates fragments, and the latter process needs to have a certain speed. Additionally, the stress drop produced by the failure causes the fragments to generate acceleration. The acceleration conversion

to speed requires a certain amount of time. Therefore, the stress drop happens before the rockburst phenomenon, and the progress time can be used as an early warning time, specifically  $\Delta T_2$  (Fig. 15a). Furthermore, Table 4 lists the early warning times of the different types of rockbursts calculated according to the two precursors. The  $\Delta T_1$  of the PUDR, the SDR and the PEDR increases successively. Thus, for rockbursts with high intensities, the early warning time is relatively short. However, in the case of  $\Delta T_2$ , the  $\Delta T_2$  values for the SDR and the PUDR are relatively small, which are one order of magnitude lower than those of the PEDR. Therefore, for practical applications, two kinds of precursors can be integrated for early warning detection. Specifically, the multifractal precursor of the AE can be applied for long-term monitoring and early warning, and the stress drop can be used for short-term monitoring and imminent warning.

### 3.7 Discussion on the Applicability and Limitation

#### 3.7.1 Applicability

AE technology is mainly used in laboratory rock mechanic tests because the common AE sensors (response frequency is larger) receive only small range of microcrack signals. However, in the field monitoring, the MS technology is usually used for rockburst warning. The precursory characteristics of rockburst were analyzed from the source parameters such as events, energy, seismic torque and apparent stress (Ma et al. 2020; Xu et al. 2022). In this paper, the experimental results of rockburst under different loading paths (SDR, PUDR,

PEDR) were compared with the field monitoring results. It is found that the multifractal parameter  $\Delta f(\alpha)$ , calculated by AE counts, increases before rockburst and decreases during rockburst, which is opposite to the variation of  $\Delta f(\alpha)$  based on the MS waveform during the coal burst (Li et al. 2017) and slope rock mass failure (Mao et al. 2020). Therefore, in terms of rockburst monitoring using multifractal of MS waveforms, the precursor should be further discussed in combination with the specific project. Additionally, Ma et al. (2018) monitored the rockburst by MS technology and found that the apparent stress has a significant downward trend before rockburst. Moreover, there was also a significant stress drop before the ejection failure of rockburst under different loading paths. Therefore, the idea of long-term monitoring and short-term early warning using multifractal and stress drop still has reference significance for field application.

### 3.7.2 Limitation

The stress paths of PUDR and PEDR designed in this paper are different from the actual conditions. The stress drops caused by small scale fault dislocation are ~3–10 MPa (Wang et al. 1995). Additionally, with the increase of distance from the fault, the stress drop will be further reduced. While during the PUDR test, the increment of pulse load is close to 150 MPa. Because the strength of the rock used in the test is much higher than that of the rock mass in the field, the best method is to equivalently convert the stress increment according to a certain similarity ratio. However, many factors should be

considered, such as the scales of the fault and the potential rockburst area, the size effect of the sample, etc., which is not conducive to simplifying the problem and revealing the rockburst mechanism. Therefore, a single pulse-type disturbance was used directly. Moreover, in addition to the stress drop caused by the fault dislocation, the local fracture of the rock mass will transmit energy in the form of seismic waves (Alcott et al. 1998), which also have influence on the trigger of rockburst. However, the influence of the seismic waves induced by the fault dislocation was not considered in this paper. Because the single pulse has made rockburst occurs. Even if there is additional seismic wave disturbance, the influence is limited.

For the PEDR, firstly, the rockburst stress is unknown. Therefore, in order to obtain the rockburst stress closest to the reality, the disturbance amplitude was increased by gradient (10 MPa, 5% of the peak stress of SDR). Secondly, for a single blasting source, the amplitude of the disturbance wave decreases with the distance from source increasing (Li et al. 2009). However, when the tunnel is continuously excavated and pushed forward by drill-blasting method, the distance between the location of blasting source and the potential rockburst area is gradually shortened, and there is an increment of disturbance amplitude. Additionally, if the tunnel advance distance is short, i.e., the blasting source is relatively fixed, the multiple blasting will also cause the accumulation of damage. The method (similar to the overload method) by gradient increasing the disturbance amplitude can approximately simulate the rockburst influenced by the cumulative damage of the rock mass (Feng et al. 2018; He et al. 2017; Hu et al. 2020).

Finally, the action direction of disturbance load was not considered in this study. The rockburst occurred at the Jinping II Hydropower Station shows that the rockburst is mainly driven by the development of rock fracture in the surrounding rock after excavation (Feng et al. 2012). If there is dynamic disturbance, the effect of disturbance will reflect in the three principal stress directions. Additionally, the existed studies have shown that the direction of the disturbance load has a significant influence on the rockburst characteristics (Liu et al. 2021). The influence of the direction, the amplitude, and the frequency of the disturbance load can be specifically studied as a topic. Moreover, Su et al. (2017c) have discussed the influence of the frequency and amplitude of the disturbance on the rockburst. However, the main focus of this paper is the influence of different stress paths on the precursory characteristics of rockburst. If the disturbance direction and

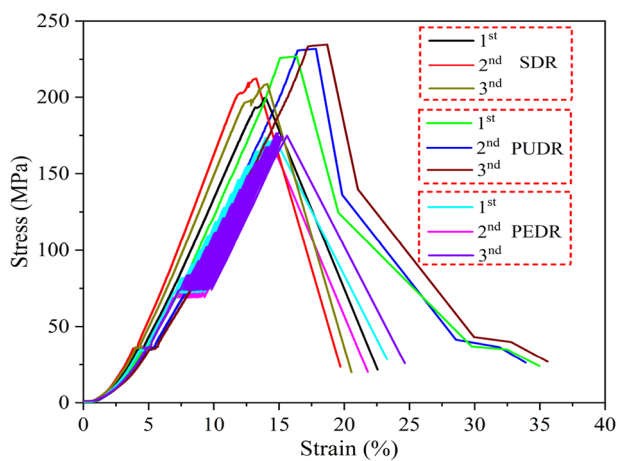


Fig. 16 Stress–strain curves (in the  $\sigma_1$  direction) of the repeated tests

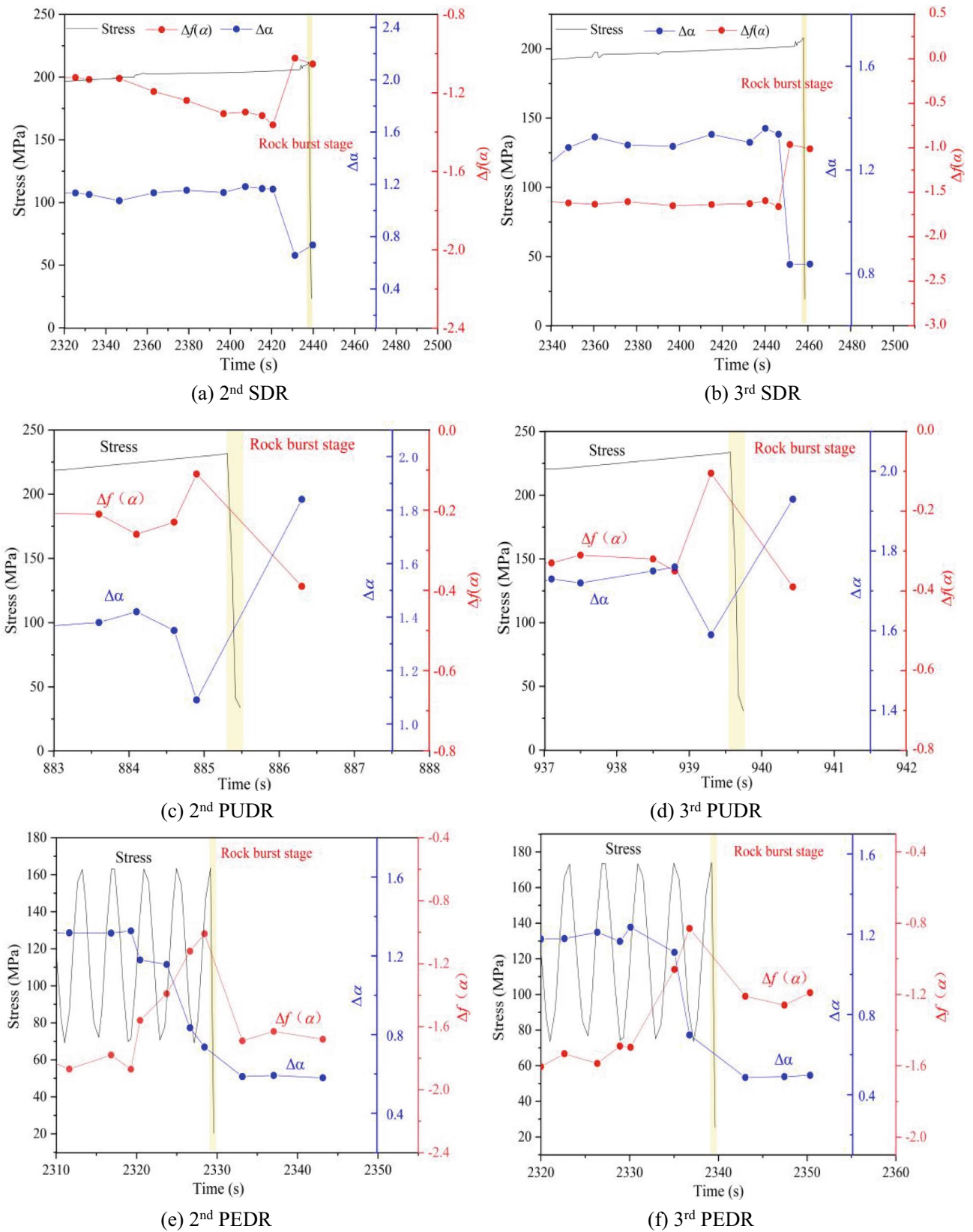


Fig. 17 The variation of AE multifractal parameters for the repeated tests



other variables are introduced, the focus of the paper will be restricted to a certain extent, and also making the paper lengthy, so it is not considered in this study.

## 4 Conclusion

In order to explore the differences between static-driven and dynamically triggered rockburst characteristics of marble, true triaxial unloading rockburst tests under three different loading modes were carried out. The characteristics of the different types of rockburst were compared and analyzed under distinct aspects, specifically stress–strain curve, energy consumption, failure mode, ejection features and AE multifractal characteristics. Finally, the reason for the obtained differences, as well as the early warning time based on the multifractal parameter and the stress drop were discussed. The main conclusions are:

1. The rockburst stresses of the PUDR, the SDR and the PEDR decrease successively, which means that the PEDR and the PUDR are the most prone and the most difficult to occur, respectively. There are yield points for the different types of rockburst stress–strain curves, but they show diverse trends after yielding. The PUDR, the SDR and the PEDR are characterized by a yield platform, strain hardening and strain softening, respectively.
2. The rockburst intensities of the PUDR, the SDR and the PEDR decrease successively, so the stress drop rate and the initial ejection velocity decrease with the same pattern; the residual stress ratio and the dissipation energy percentage during the rockburst stage increase successively.
3. The multifractal spectra characteristics of the AE indicate that the PUDR AE signals have the most violent fluctuations, while the SDR ones involve more high energy signals. However, the PEDR AE signals have fewer fluctuations and possess fewer high energy signals.
4. The rockburst stages of the PUDR, the SDR and the PEDR are dominated by tensile micro-cracks, and the tension effect increases successively. The AE b-values for the PUDR and the SDR denote a downward trend, indicating that the stress inside the sample is continuously concentrated after the ejection process. However, the PEDR b-values vary in the form of fluctuations, indicating that stress release and concentration occur alternately.
5. The initial increase and then decrease of the AE multifractal parameter  $\Delta f(\alpha)$  can be used as the precursor of different types of rockburst. The early warning time is related to the rockburst intensity, which implies that greater intensity values indicate a shorter early warning

time. Additionally, the stress drop can be used as a short-term and imminent prediction precursor of rockburst. For rockbursts with similar intensities (both strong), the early warning time is close, but they are shorter than the early warning time of weak rockbursts.

## Appendix A: The Repeatability of the rockburst tests

In order to ensure the reliability of the results, the repeatability tests were carried out. As shown in Fig. 16, the peak stresses of the three tests under the different loading paths are closed, which are 199.5–212.2 MPa (SDR), 226.8–233.9 MPa (PUDR), 163.9–174.2 MPa (PEDR), respectively. From the perspective of multifractal, as shown in Fig. 17, the variation of multifractal parameters of three samples under each loading path is consistent during the rockburst stage.

**Acknowledgements** Financial support from the National Key Research and Development Program of China (2022YFC3080100), the National Natural Science Foundation of China (Grant No. 52104125), the open fund of State Key Laboratory for GeoMechanics and Deep Underground Engineering Beijing (Grant No. SKLGDUEK2128), the open fund of State Key Laboratory of Geomechanics and Geotechnical Engineering (Grant No. KFJJ-2022-4), and University of Science and Technology, LiaoNing (Grant No. 2021YQ02), the fund of Young Elite Scientists Sponsorship Program by CAST (Grant No. 2021QNRC001), Natural Science Foundation of Liaoning Province (Grant No. 2022-BS-280), and China Scholarship Council are gratefully acknowledged.

**Data Availability** All data used during the study are available from the corresponding author by request.

## Declarations

**Conflict of interest** The authors declared that there is no conflict of interest to this work.

## References

- Alcott JM, Kaiser PK, Simser BP (1998) Use of microseismic source parameters for rockburst hazard assessment. *Pure Appl Geophys* 153:41–65
- Amoussou CA, Candan G, Wu L et al (2013) Knowledge-based and data-driven fuzzy modeling for rockburst prediction. *Int J Rock Mech Min Sci* 61(4):86–95
- Cai M, Kaiser PK (2018) Rockburst support reference book Volume I: rockburst phenomenon and support characteristics. Laurentian University and Mirarco Mining Innovation
- Chen BR, Feng XT, Li QP et al (2015) Rock Burst intensity classification based on the radiated energy with damage intensity at Jinping II Hydropower Station, China. *Rock Mech Rock Eng* 48:289–303

- Cheng C (2011) Influence of homogeneity of rock material on rockburst based on numerical analysis. Second International Conference on Mechanic Automation & Control Engineering, IEEE
- Dai F, Xia KW, Tang LZ (2010) Rate dependence of the flexural tensile strength of laurentian granite. *Int J Rock Mech Min Sci* 47(3):469–475
- Dai F, Li B, Xu NW et al (2017) Microseismic early warning of surrounding rock mass deformation in the underground powerhouse of the Houziyan hydropower station, China. *Tunn Undergr Space Technol* 62:64–74
- Du K, Tao M, Li XB et al (2016) Experimental study of slabbing and rockburst induced by true-triaxial unloading and local dynamic disturbance. *Rock Mech Rock Eng* 49(9):3437–3453
- Feng XT, Chen BR, Feng GL et al (2018) Description of rockbursts in tunnels. In: Feng XT (ed) *Rockburst: mechanisms, monitoring, warning and mitigation*. Butterworth-Heinemann, Oxford, pp 3–19
- Feng XT, Xiao YS, Feng GL (2012) Mechanism, warning and dynamic control of rockburst development processes. SRM Regional Symposium—7th Asian Rock Mechanics Symposium 2012, pp 26–34
- Gong QM, Yin LJ, Wu SY et al (2012) Rock burst and slabbing failure and its influence on TBM excavation at headrace tunnels in Jinping II hydropower station. *Eng Geol* 124:98–108
- Gong FQ, Wu WX, Li TB (2019) Experimental simulation and investigation of spalling failure of rectangular tunnel under different three-dimensional stress states. *Int J Rock Mech Min Sci* 122:104081
- Gong FQ, Ni YX, Ren L (2022) Effects of loading rate on rockburst proneness of granite from energy storage and surplus perspectives. *Rock Mech Rock Eng* 55:6495–6516
- He MC, Miao JL, Feng JL (2010) Rock burst process of limestone and its acoustic emission characteristics under true-triaxial unloading conditions. *Int J Rock Mech Min Sci* 47(2):286–298
- He MC, Nie W, Zhao ZY et al (2012) Experimental investigation of bedding plane orientation on the rockburst behavior of sandstone. *Rock Mech Rock Eng* 45(3):311–326
- He J, Dou LM, Gong SY et al (2017) Rock burst assessment and prediction by dynamic and static stress analysis based on micro-seismic monitoring. *Int J Rock Mech Min Sci* 93:46–53
- He MC, Ren FQ, Liu DQ (2018) Rockburst mechanism research and its control. *Int J Min Sci Technol* 28(05):116–124
- Hu SB, Wang EY, Li ZH et al (2014) Time-Varying multifractal characteristics and formation mechanism of loaded coal electromagnetic radiation. *Rock Mech Rock Eng* 47:1821–1838
- Hu LH, Ma K, Liang X et al (2018) Experimental and numerical study on rockburst triggered by tangential weak cyclic dynamic disturbance under true triaxial conditions. *Tunn Undergr Space Technol* 81:602–618
- Hu LH, Li YC, Liang X et al (2020) Rock damage and energy balance of strainbursts induced by low frequency seismic disturbance at high static stress. *Rock Mech Rock Eng* 53:4857–4872
- Hu LH, Liang X, Liang ZZ et al (2021) Influence of radial stress on strainbursts under true triaxial conditions: insights from a distinct element modelling. *Int J Rock Mech Min Sci* 138(9):104577
- Huo MZ, Xia YY, Liu XQ et al (2020) Evolution characteristics of temperature fields of rockburst samples under different stress gradients. *Infrared Phys Technol* 109(5):103425
- Kong B, Wang EY, Li ZH et al (2016a) Nonlinear characteristics of acoustic emissions during the deformation and fracture of sandstone subjected to thermal treatment. *Int J Rock Mech Min Sci* 90:43–52
- Kong XG, Wang EY, Hu SB et al (2016b) Fractal characteristics and acoustic emission of coal containing methane in triaxial compression failure. *J Appl Geophys* 124:139–147
- Kong XG, Wang EY, He XQ et al (2017) Time-varying multifractal of acoustic emission about coal samples subjected to uniaxial compression. *Chaos, Solitons Fractals* 103:571–577
- Kong XG, Wang EY, Li SG et al (2019) Fractals and chaos characteristics of acoustic emission energy about gas-bearing coal during loaded failure. *Fractals* 27(05):1950072
- Li XB, Ling TH, Zhang YP (2009) *Analysis of blast vibration signals theories and methods*. Science Press, Beijing
- Li SJ, Feng XT, Li ZH et al (2012) In situ monitoring of rockburst nucleation and evolution in the deeply buried tunnels of Jinping II hydropower station. *Eng Geol* 137–138:85–96
- Li DJ, Zhao F, Zheng M (2014) Fractal characteristics of cracks and fragments generated in unloading rockburst tests. *Int J Min Sci Technol* 24(6):819–823
- Li N, Li BL, Chen D et al (2017) Multi-fractal and time-varying response characteristics of microseismic waves during the rockburst process. *J China Univ Min Technol* 46(5):1007–1013 ((in Chinese))
- Li XL, Li ZH, Wang EY et al (2018a) Pattern recognition of mine microseismic and blasting events based on wave fractal features. *Fractals* 26(03):1850029
- Li H, Zhong ZL, Liu XR, Sheng Y, Yang DM (2018b) Micro-damage evolution and macro-mechanical property degradation of limestone due to chemical effects. *Int J Rock Mech Min Sci* 110:257–265
- Li PX, Feng XT, Feng GL et al (2019) Rockburst and microseismic characteristics around lithological interfaces under different excavation directions in deep tunnels. *Eng Geol* 260:105209
- Lin MQ, Gao CC, Xia YY et al (2022) Rock burst initiation and precursors in a model specimen based on acoustic emission and infrared monitoring. *Arab J Geosci* 15(4):1–19. <https://doi.org/10.1007/s12517-021-09423-y>
- Liu F, Ma TH, Tang CA et al (2018a) Prediction of rockburst in tunnels at the Jinping II hydropower station using microseismic monitoring technique. *Tunn Undergr Space Technol* 81:480–493
- Liu XX, Liang ZZ, Zhang YB et al (2018b) Experimental study on the monitoring of rockburst in tunnels under dry and saturated conditions using AE and infrared monitoring. *Tunn Undergr Space Technol* 82:517–528
- Liu DQ, Han ZJ, Wang CG et al (2021) Experimental study on fragment characteristics of rockburst induced by uni-directional, bi-directional and tri-directional disturbances. *J Central South Univ (Sci Technol)* 52(8):2793–2804 ((in Chinese))
- Liu J, Li Q, Wang X et al (2022) Dynamic multifractal characteristics of acoustic emission about composite coal-rock samples with different strength rock. *Chaos, Solitons & Fractals*, 164, 112725
- Lou S, Song SZ, He XQ et al (2019) Correlations between acoustic and electromagnetic emissions and stress drop induced by burst-prone coal and rock fracture. *Saf Sci* 115:310–319
- Lu CP, Liu Y, Zhang N et al (2018) In-situ and experimental investigations of rockburst precursor and prevention induced by fault slip. *Int J Rock Mech Min Sci* 108:86–95
- Luo Y, Gong FQ, Si XF et al (2019) Experimental simulation analysis of the process and failure characteristics of spalling in D-shaped tunnels under true-triaxial loading conditions. *Tunn Undergr Space Technol* 90:42–61
- Luo JW, Zhang DL, Fang Q et al (2021) Mechanical responses of surrounding rock mass and tunnel linings in large-span triple-arch tunnel. *Tunn Undergr Space Technol* 113:103971
- Ma CC, Li TB, Zhang H et al (2018) An evaluation and early warning method for rockburst based on EMS microseismic source parameters. *Rock Soil Mech* 39(2):765–774 ((in Chinese))
- Ma CC, Li TB, Zhang H (2020) Microseismic and precursor analysis of high-stress hazards in tunnels: a case comparison of rockburst and fall of ground. *Eng Geol* 265:105435

- Mao HY, Zhang M, Li B et al (2020) Stability analysis of the left bank slope of baihetan hydropower station based on the MF-DFA method. *Adv Civil Eng* 2020:8898318
- Qiu LM, Song DZ, He XQ et al (2020) Multifractal of electromagnetic waveform and spectrum about coal rock samples subjected to uniaxial compression. *Fractals* 28(5):2050061
- Ren FQ, Zhu C, He MC (2020) Moment tensor analysis of acoustic emissions for cracking mechanisms during schist strain burst. *Rock Mech Rock Eng* 53(1):153–170
- Sayed NAE, Abuseda H, Kassab MA (2015) Acoustic wave velocity behavior for some Jurassic carbonate samples, north Sinai. *Egypt J Afr Earth Sci* 111:14–25
- Schorlemmer D, Wiemer S, Wyss M (2005) Variations in earthquake-size distribution across different stress regimes. *Nature* 437:539–542. <https://doi.org/10.1038/nature04094>
- Su GS, Chen ZY, Ju JW et al (2017a) Influence of temperature on the strainburst characteristics of granite under true triaxial loading conditions. *Eng Geol* 222:38–52
- Su GS, Shi YJ, Feng XT et al (2017b) True-triaxial experimental study of the evolutionary features of the acoustic emissions and sounds of rockburst processes. *Rock Mech Rock Eng* 51:375–389
- Su GS, Feng XT, Wang JH et al (2017c) Experimental study of remotely triggered rockburst induced by a tunnel axial dynamic disturbance under true-triaxial conditions. *Rock Mech Rock Eng* 50:2207–2226
- Sun XM, Xu HC, Zheng LG et al (2016) An experimental investigation on acoustic emission characteristics of sandstone rockburst with different moisture contents. *SCIENCE CHINA Technol Sci* 59:1549–1558
- TamásT AM, Celso G, György K (2005) Chemical and biological activity in open flows: a dynamical system approach. *Phys Rep* 413(2–3):91–196
- Tang SB, Wang JX, Tang CA (2021) Identification of microseismic events in rock engineering by a convolutional neural network combined with an attention mechanism. *Rock Mech Rock Eng* 54:47–69
- Wang K, Mulder T, Rogers GC et al (1995) Case for very low coupling stress on the Cascadia Subduction Fault. *JGR Solid Earth* 100:12907–12918
- Wang JM, Zeng XH, Zhou JF (2012) Practices on rockburst prevention and control in headrace tunnels of Jinping II hydropower station. *J Rock Mech Geotech Eng* 4(3):258–268
- Wang JX, Tang SB, Heap MJ et al (2021a) An auto-detection network to provide an automated real-time early warning of rock engineering hazards using microseismic monitoring. *Int J Rock Mech Min Sci* 140:104685
- Wang ZY, Wu ZJ, Fan LF et al (2021b) An improved wave velocity model for acoustic emission source localization in heterogeneous rock materials with unknown inclusions. *J Eng Mech* 148:04021122
- Xu FL, Wang EY, Song DZ et al (2011) Long-range correlation and multifractal distribution of acoustic emission of coal-rock. *Rock Soil Mech* 32(07):2111–2116
- Xu K, Song LB, Song WJ et al (2022) Research on temporal and spatial distribution characteristics of microseismic events of slip-type rockburst. *Shock Vib* 2022(05):1–15
- Yan J, He C, Wang B et al (2019) Inoculation and characters of rockbursts in extra-long and deep-lying tunnels located on Yarlung Zangbo suture. *Chin J Rock Mech Eng* 38(4):769–781 ((in Chinese))
- You W, Dai F, Liu Y et al (2021) Investigation of the influence of intermediate principal stress on the dynamic responses of rocks subjected to true triaxial stress state. *Int J Mining Sci Technol* 31(5):913–926
- Yue JG, Kunnath SK, Xiao Y (2020) Uniaxial concrete tension damage evolution using acoustic emission monitoring. *Constr Build Mater* 232:117281. <https://doi.org/10.1016/j.conbuildmat.2019.117281>
- Zhang R, Zhu SY, Sun Q et al (2015) Fractal characteristics of limestone after high temperature under uniaxial compression. *China Earthq Eng J* 37(2):541–545 ((in chinese))
- Zhang C, Li XB, Dong LJ et al (2016) Intelligent prediction of rock mass instability based on microseismic monitoring. *J Safety Sci Technol* 12(03):5–9 ((in Chinese))
- Zhang ZB, Wang EY, Zhao EL et al (2018) Nonlinear characteristics of acoustic emission during the heating process of coal and rock. *Fractals* 26(04):1850046
- Zhang R, Liu J, Sa ZY et al (2020) Experimental investigation on multifractal characteristics of acoustic emission of coal samples subjected to true triaxial loading–unloading. *Fractals* 28(05):2050092
- Zhao XG, Cai M (2014) Influence of specimen height-to-width ratio on the strainburst characteristics of tianhu granite under true-triaxial unloading conditions. *Can Geotech J* 52(7):890–902
- Zhou ZL, Cai X, Li XB et al (2020) Dynamic response and energy evolution of sandstone under coupled static–dynamic compression: insights from experimental study into deep rock engineering applications. *Rock Mech Rock Eng* 53(3):1305–1331

**Publisher's Note** Springer Nature remains neutral with regard to jurisdictional claims in published maps and institutional affiliations.

Springer Nature or its licensor (e.g. a society or other partner) holds exclusive rights to this article under a publishing agreement with the author(s) or other rightsholder(s); author self-archiving of the accepted manuscript version of this article is solely governed by the terms of such publishing agreement and applicable law.